CrossMark

CAMBRIDGE
UNIVERSITY PRESS

Research Article

First photometric and orbital period investigations of four W UMa-type eclipse binaries

Ke Hu[1,2] , Zi-Bin Meng[1], Hong-Wei Wang[1], Yun-Xia Yu[1,2] and Fu-Yuan Xiang[1,2]

[1]Key Laboratory of Star and Interstellar Medium, Xiangtan University, Xiangtan, Hunan 411105, China and [2]Department of Physics, Xiangtan University, Xiangtan, Hunan 411105, China

Abstract

We presented the first photometric and orbital period investigations for four W Ursae Majoris-type binaries: V473 And, V805 And, LQ Com, and EG CVn. The photometric solutions suggested that V805 And and LQ Com are two total-eclipse contact binaries, while V473 And and EG CVn are partial-eclipse ones. V473 And and LQ Com belong to the A-subtype contact binaries, while V805 And and EG CVn belong to the W subtype. The O'Connell effects found in the light curves of V805 And, LQ Com, and EG CVn can be interpreted as a result of a cool spot on the surface of their less massive and hotter primary components. Based on two different methods, the absolute physical parameters were properly determined. Combining the eclipse timings derived from our observations and survey's data with those collected from literature, we investigated their orbital period variations. The results show that the orbital periods of V473 And, V805 And, and EG CVn are undergoing a secular decrease/increase superposed a periodic variation, while LQ Com exhibits a possible cyclic period variation with a small amplitude. The secular period changes are caused mainly by the mass transfer between two components, while the cyclic period oscillations may be interpreted as the results of either the light-time effect due to the third body or the cyclic magnetic activity. Finally, we made a statistical investigation for nearly 200 contact binaries with reliable physical parameters. The statistical results suggested that the W-subtype systems are more evolved than the A-subtype ones. Furthermore, the evolutionary direction of A-subtype into W-subtype systems is also discussed. The opposite evolutionary direction seems to be unlikely because it requires an increase of the total mass, the orbital angular momentum, and the temperature differences between two components of a binary system.

Keywords: stars: binaries: close – stars: binaries: eclipsing – stars: evolution – stars: individual (V473 And, V805 And, LQ Com, EG CVn)

(Received 2 March 2022; revised 29 September 2022; accepted 10 October 2022)

1. Introduction

Among the big family of close binaries, W Ursae Majoris (W UMa)-type contact binaries are the most frequently observed and intensively investigated type of eclipse binaries (Mochnacki 1981; Rucinski 1998, 2000). A contact binary consists of two components sharing a common convective envelope (Lucy 1968). The shape looks just like a dual-core peanut. Usually, this type of systems have the spectral type of F, G, or K (Rucinski 1993), and the orbital period mainly distributes between 0.2 and 1.0 d (Paczyński et al. 2006). Because of mass and energy exchanges, two components of a contact binary often have almost equal surface temperatures although their masses may be typical unequal. The amplitudes of luminosity variations yielded by eclipse are, in general, less than 0.8 mag in the V band. In order to insight the basic observational features (Rucinski 1985, 1993), the properties of the common envelope (Lucy 1973), the physical processes of the mass and energy exchange between two components (Kähler 2002, 2004), and the internal structures of component stars (Webbink 2003; Li, Han, & Zhang 2004), have been also widely investigated over the past half century.

Although contact binaries are the largest part of stellar population, their formation, evolution, and final destinations are still not well understood. In formation process, a triple or multiple system seems to be a necessary stage, because it involves the Kozai mechanism with tidal frictions (Kozai 1962; Kiseleva, Eggleton, & Mikkola 1998; Fabrycky & Tremaine 2007). However, the statistical results (Tokovinin et al. 2006; Eggleton & Tokovinin 2008) suggested that not all of contact binaries are indeed the members of triple or multiple star systems. In the contact phase, the W UMa-type contact binaries have been further divided into two subtypes: A- and W-subtype (Binnendijk 1970). The physical parameters for two different subtypes show different statistical characteristics (Rucinski 1974; Smith 1984; Yakut & Eggleton 2005; Gazeas & Niarchos 2006; Gazeas & Stępień 2008). Maceroni & van't Veer (1996) pointed out that these differences are not only related to the light-curve morphology, but also have an underlying implication to both evolutionary state or origin. Weather do both A- and W-subtype contact binaries have the same progenitor, or not? Can do the one subtype evolve to the other? These problems are still not clear. Finally, both the evolutionary theories (Darwin 1908; Counselman 1973; Webbink 1976; Hut 1980), extensive simulations (Han et al. 2002; Andronov, Pinsonneault, & Terndrup 2006; Li et al. 2008; Yıldız 2014), and statistical analyses (Qian et al. 2006; Gazeas & Stępień 2008; Yang & Qian 2015) suggested a contact binary may evolve into the single and rapidly rotating star via merger. However, only one

merging event of contact binary, i.e., the red nova event of V1309 Sco (Tylenda et al. 2011; Zhu et al. 2016), has been observed so far. These open problems make contact binaries one of the most intriguing objects in stellar astrophysics (Eggleton 2012), and could, perhaps, be solved by accumulating enough knowledge of the fundamental physical parameters for a large number of such samples.

In this work, we presented the first photometric and orbital period investigations for four W UMa-type contact binaries: V473 And, V805 And, LQ Com, and EG CVn. Among them, V473 And (=GSC 02790-00068) was discovered by Kuzmin (2008) with the archive data of the Northern Sky Variability Survey (NSVS,[a] Woźniak et al. 2004), where the orbital period of 0.40136 d and the *R*-band magnitude range from 13.8 to 14.3 were estimated. V805 And (=SvkV38 And, UCAC3 274-028768) was discovered by Vrastak (2015) using the 0.24 m Newton reflector telescope at the Liptovská Štiavnica Observatory. It is a relatively dark source with the mean magnitude of $14^m.716$ and the amplitude of $0^m.75$ in *V* band. The orbital period is 0.44394 d (Vrastak 2015). LQ Com (=ROTSE1 J123730.26 260451.8, GSC 01990-01198) and EG CVn (=ROTSE1 J133726.05 373458.4, GSC 03026-01046) were discovered by Akerlof et al. (2000) with the first-generation Robotic Optical Transient Search Experiment (ROTSE1) telescope. Based on the ROTSE1 survey's data, Diethelm (2001) calculated the phase-folded light curve of LQ Com according to the ROTSE1 period of 0.35684 d, and derived two eclipse timings with the Kwee-Van Woerden (K-W) method (Kwee & van Woerden 1956). EG CVn was later observed by Blattler & Diethelm (2002) using private 0.15 m Starfire refractor telescope with SBIG ST-7 CCD camera, where the orbital period was determined as 0.349271 d and a complete light curve without filter was presented. Together with the ROTSE1 observations, Blattler & Diethelm (2002) also derived a total of 12 eclipse timings using the K-W method.

Besides the photometric observations mentioned above, the four binary systems were scanned by several time-domain surveys, such as the Catalina Real-Time Transient Survey (CRTS,[b] Drake et al. 2009), the Wide Angle Search for Planets (WASP,[c] Butters et al. 2010), the All-Sky Automated Survey for SuperNovae (ASAS-SN,[d] Shappee et al. 2014; Jayasinghe et al. 2019), the Transiting Exoplanet Survey Satellite (TESS, Ricker et al. 2015), and the Zwicky Transient Facility (ZTF,[e] Masci et al. 2019; Bellm et al. 2019). In particular, based on the photometric data of ASAS-SN, Jayasinghe et al. (2018) further corrected their orbital periods using a comprehensive approach involving the Generalised Lombe-Scargle, the Multi-Harmonic Analysis of Variance, the Phase Dispersion Minimisation, and the Box Least Squares periodograms. Although these surveys' photometric observations were discontinuous and of low precision, they distributed over a wide time interval and can provide some phase-folded light curves to estimate the preliminary light-curve types and determine some eclipse timings. In addition, three targets (i.e., V473 And, LQ Com, and EG CVn) are recently observed in Sector 23 with a 30-min cadence by TESS. TESS is a space-based telescope launched in 2018 April and placed in a highly elliptical orbit with a period of 13.7 d. These three targets were continuously, but long-cadence,

Table 1. Log of photometric observations for four target stars.

Target	Telescope	UT Date	Exposure time (s)	Number of Images
V473 And	85-cm	2016 Dec. 04	85,65,42	78,76,74
		2016 Dec. 05	90,70,60	89,88,88
		2017 Nov. 29	90,50,40	106,106,106
		2017 Nov. 30	60,30,30	97,97,97
V805 And	85-cm	2018 Nov. 24	80,35,20	177,176,177
		2018 Nov. 25	100,50,25	172,171,170
		2020 Nov. 10	55,25,15	206,205,203
		2020 Nov. 12	70,37,30	202,201,200
LQ Com	60-cm	2020 Apr. 26	40,30,20	199,212,212
		2021 Mar. 29	200,150,120	43,43,43
		2021 Apr. 18	200,150,120	54,56,57
EG CVn	85-cm	2015 Apr. 28	45,35,15	228,236,234
		2015 Apr. 29	45,35,15	34,29,31

monitored in 2019 for a cycle (two elliptical orbit periods, 27.4 d), with a break near the midpoint for downlink of data to Earth. These high-precision photometric data will be very helpful for deriving the light-curve solutions more firmly.

On the side of spectroscopic observation, all of them have been scanned by the *Gaia* mission[f] (Gaia Collaboration et al. 2016, 2018), and some spectroscopic elements were well revealed. Combining these surveys' information with our high-precision and multi-colour photometric observations, we performed the detailed photometric and orbital period investigations for the four contact binaries, aiming to determine their absolute physical parameters and to uncover their photometric natures and evolutionary states.

2. Photometric observations

The four eclipse binaries were observed using the 60 and 85-cm telescopes at Xinglong station of National Astronomical Observatories of China (NAOC). During the observations, the Andor DZ936 PI2048 CCD photometric system was equipped and the standard Johnson-cousins *BVR* filters were adopted. The observation information (e.g., date, exposure time, and number of images) are summarised in Table 1. All images are reduced to photometric data using the aperture photometry package from the Image Reduction and Analysis Facility (IRAF[g]) software library. From their respective fields of view, we selected two stars with the locations, magnitudes, and colours as close to those of the targets as possible, as their comparison and check stars. By checking the magnitude differences between the comparison and check stars, we confirmed that the photometric luminosity between them is stable throughout the observations. From the Set of Identifications, Measurements and Bibliography for Astronomical Data (SIMBAD) database and the latest data release (DR9) of AVVSO Photometric All Sky Survey (Henden et al. 2015), the coordinates and magnitudes in *B* and *V* band were collected. From the *Gaia* DR2, we extracted the parallaxes.

Table 2. Coordinates, magnitudes and parallaxes of target, comparison, and check stars.

| Object	Period (d)	α_{2000}	δ_{2000}	B (mag)	V (mag)	Parallax (mas)
V473 And	0.4012974	$00^h16^m05.38^s$	$41°51'24.11''$	14.11	13.67	0.846(0.016)
TYC 2790-762-1		$00^h15^m41.29^s$	$41°54'57.33''$	13.25	12.76	4.503(0.031)
TYC 2790-622-1		$00^h15^m38.61^s$	$41°41'56.93''$	13.10	12.15	2.146(0.033)
V805 And	0.4439421	$02^h10^m25.37^s$	$46°45'20.85''$	15.81	15.02	0.648(0.029)
AP2418966		$02^h10^m28.57^s$	$46°45'45.48''$	15.42	14.90	0.456(0.054)
AP2418956		$02^h10^m30.45^s$	$46°44'55.18''$	15.75	15.02	0.619(0.056)
LQ Com	0.3568355	$12^h37^m30.28^s$	$26°04'52.12''$	13.16	12.77	1.649(0.041)
AP27635668		$12^h37^m14.18^s$	$26°03'59.98''$	13.96	13.02	5.312(0.039)
AP27635667		$12^h37^m11.37^s$	$26°00'13.67''$	13.35	12.76	1.708(0.038)
EG CVn	0.3492761	$13^h37^m26.21^s$	$37°34'59.65''$	13.53	13.00	1.487(0.013)
TYC 3026-922-1		$13^h37^m21.38^s$	$37°38'08.50''$	12.61	11.56	2.179(0.028)
TYC 3026-979-1		$13^h37^m11.23^s$	$37°35'15.34''$	13.26	11.96	0.561(0.025)
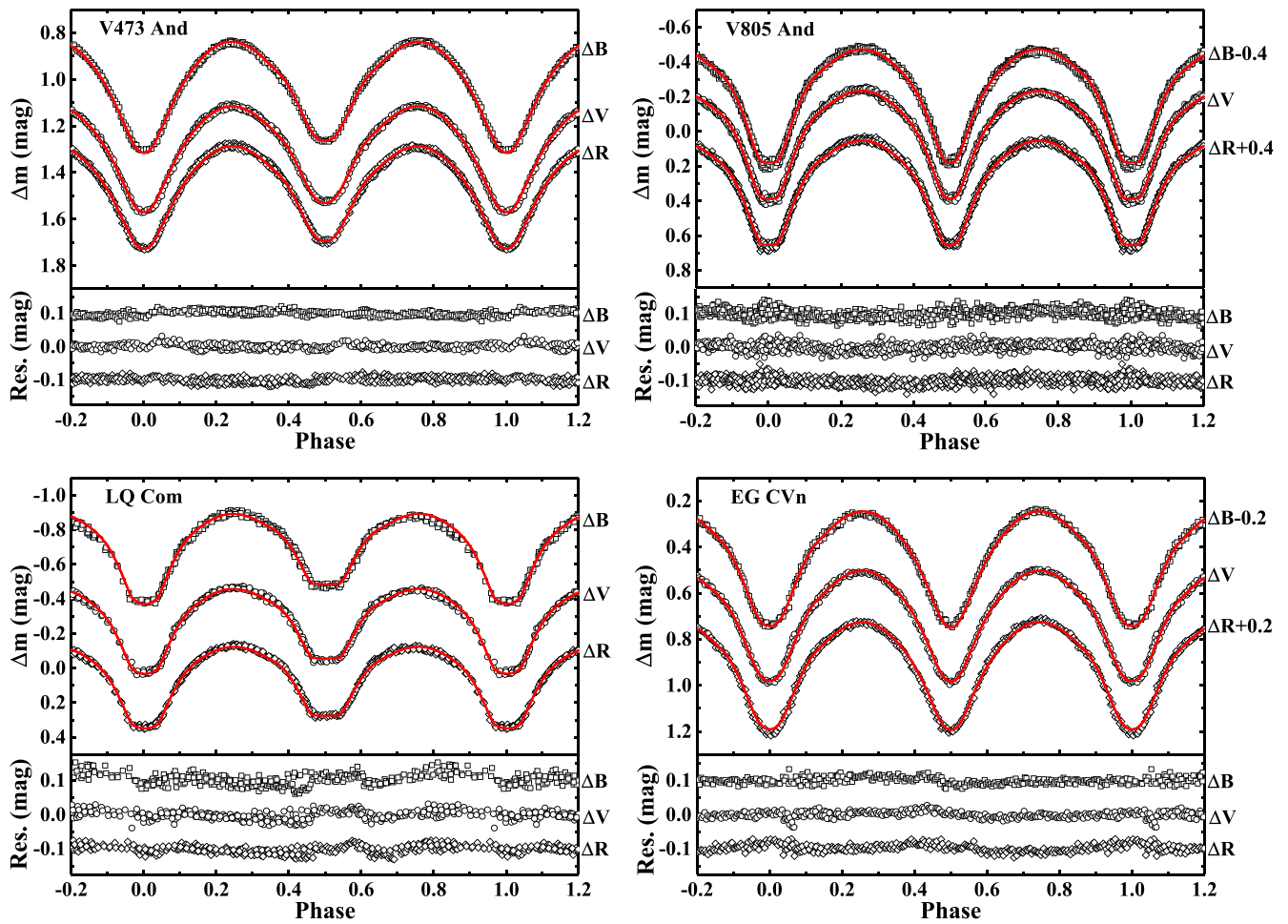
Figure 1. Top of each panel: Observed (symbols) and theoretical (solid lines) light curves without spot for four targets: V473 And, V805 And, LQ Com, and EG CVn. Bottom: the corresponding residuals (the residuals for *B* and *R* bands are vertically shifted by 0.1 and −0.1 mag, respectively).

All these information for the targets, comparison, and check stars are compiled in Table 2. The reduced data are presented in the form of different magnitude between the target and comparison stars, and the phases are calculated using the orbital periods (the second column of Table 2) determined by Jayasinghe et al.

(2018). The photometric data, including the Heliocentric Julian Day (HJD), phases, and different magnitudes, are compiled as the Supplementary File (see Tables S1–S4 of Appendix A).

The phase-folded light curves for each of our targets are displayed in Figure 1. All of the four binary systems show the typical

EW-type luminosity variation, indicating they are in contact or near-contact configuration. In addition, the light curves of LQ Com show a very wide flatness around both the primary and secondary eclipses, especially for the secondary eclipse (the constant luminosity sustains about 0.08 phase, i.e., about 40 min). This implies that LQ Com is a total-eclipse binary and the radius of its hot primary component is significantly larger than that of the cool secondary one. The slight and symmetric distortion of the primary-eclipse flatness should mainly attribute to the limb darkening effect of the primary component. Combining the wider flatness around the primary eclipse with the fact that the primary eclipse is deeper than the secondary eclipse, we can infer that LQ Com is an A-subtype and total-eclipse binary. For V805 And, a narrow flatness appears on the deeper primary eclipse, but disappear for the somewhat shallow secondary eclipse. This means that V805 And should be also a total-eclipse binary, but belongs to the W-subtype. The sharp light minima for both V473 And and EG CVn indicate that they should be two partial-eclipse binaries.

3. Photometric solutions and absolute parameters

The Wilson–Devinney (W–D) code (Wilson & Devinney 1971; Wilson 1979, 1990; Wilson & Van Hamme 2014) is one of the most customary programmes to model the observed light and radial velocity curves of various binary systems. It has been revised and improved for many times. Here the latest 2015 version of W–D code is adopted to analyse the multi-band light curves of the four binaries: V473 And, V805 And, LQ Com, and EG CVn. Firstly, we estimate the effective temperatures of their primary components according to two available colour indices ($B-V$ and $J-K$) and the *Gaia* spectroscopic observations. The $B-V$ and $J-K$ colour indices are collected from the AVVSO Photometric All Sky Survey[h] (Henden et al. 2015) and the Two Micron All Sky Survey[i] (Skrutskie et al. 2006), respectively. The corresponding temperatures, T_{BV} and T_{JK}, are estimated with the corrected calibration[j] (Pecaut & Mamajek 2013). The colour indices and the effective temperatures estimated from them and the *Gaia* spectroscopic observations, are summarised in Table 3. The average values of three temperatures are presented in the last column of Table 3, and the corresponding errors are denoted by the standard deviations. In fact, the average value could not represent exactly the temperature of the primary component, and should be a quadrature temperature of the two components. However, because the temperatures of two components, in general, do not significantly deviate from each other for a typical W UMa-type contact binary, we adopted the average temperature as a preliminary one T_{pre} of the primary and the final temperatures for both primary and secondary would be adjusted according to the following equations (Kjurkchieva & Vasileva 2015),

$$T_1^f = T_{pre} + \frac{c\Delta T}{c+1}, T_2^f = T_1^f - \Delta T, \qquad (1)$$

where $c = l_2/l_1$, denotes the relative luminosity ratio of two components, and $\Delta T = T_{pre} - T_2$. The gravity darkening and bolometric albedos coefficients of the components were set to be $g_1 = g_2 = 0.32$ (Lucy 1967) and $A_1 = A_2 = 0.5$ (Ruciński 1969), respectively. For the bolometric and bandpass-specific limb

Table 3. Colours, and temperatures of V473 And, V805 And, LQ Com, and EG CVn.

Name	$B-V$	$J-K$	T_{BV}	T_{JK}	T_G	T_{pre}
V473 And	0.43	0.30	6553	6051	6473	6359 ± 220
V805 And	0.79	0.41	5310	5560	5334	5401 ± 112
LQ Com	0.40	0.29	6680	6170	6226	6359 ± 228
EG CVn	0.53	0.31	6170	6020	6553	6248 ± 224

darkening law, we selected the square root law (Diaz-Cordoves & Gimenez 1992). The corresponding coefficients were interpolated from the table of Claret & Bloemen (2011). Of course, these coefficients will be modified when the temperatures are adjusted. The four targets show the typical EW-type light curves, suggesting they should be contact binaries. Thus, we selected the mode 3, i.e., the contact model, in the W–D code. Some other parameters, e.g., the mass ratio q, the orbital inclination i, the secondary's temperature T_2, the primary's monochromatic luminosity L_1, and the dimensionless potential $\Omega_1 = \Omega_2$ of two components, are set as the free ones. The secondary's monochromatic luminosity L_2 is calculated according to the blackbody radiation model.

Because neither spectroscopic nor photometric mass ratios have been reported for these four binaries so far, we employed the q−search method to estimate their initial mass ratios. In the numerical scheme, we calculated Chi square $\chi^2 = \frac{1}{n} \sum_i w_i (O_i - C_i)^2$ for the optimal fit of light curves at a series of fixed mass ratios q, with the values ranging from 0.20 to 5.0 in step of 0.1. For V473 And and LQ Com, finer grid search at increment of 0.01 for the value of q was conducted near the approximate value to obtain the more accurate values of their initial mass ratios. Figure 2 displayed the relation between Chi square χ^2 and mass ratio $q = M_2/M_1$. Clearly, there are two minima for LQ Com, and one minimum for the other three targets. The first minimum for LQ Com appears at $q = 0.26$, and the second minimum is at $q = 4.2$. As has been mentioned, we could determine that LQ Com is an A-subtype contact binary from the light-curve morphology. Moreover, χ^2 for the first minimum is smaller than that for the second minimum. Thus the mass ratio of LQ Com should be about 0.26. According to the criteria for the reliability of photometric mass ratio proposed by Zhang et al. (2017b), the sharper of the minimum in the q−search curve, the more reliable the photometric mass ratio. Both V473 And and LQ Com show a very sharper minimum in their q−search curves, but the minima for V805 And and EG CVn are relatively flat. This implies that the photometric mass ratios for V473 And and LQ Com are more reliable than those of V805 And and EG CVn. However, according to the statistical analysis of Pribulla et al. (2003) and the numerical simulations of Terrell & Wilson (2005), photometric mass ratio should be reliable for total-eclipse contact binaries. Thus, in spite of the flat minimum of the q−search curve for V805 And, its mass ratio determined from the photometric light curves, would be still reliable. Comparatively, the mass ratio of EG CVn should be unreliable due to both the partial eclipse and the flat minimum in the q-search curve.

Based on the above settings of parameters and the initial mass ratios, we run the W–D code to simultaneously solve the multi-band light curves. After achieving the optimal converging solutions via enough iterations, we modified the temperatures of the primary and secondary components according to Equation (1), and rerun the W–D code to obtain the final and self-consistent converging
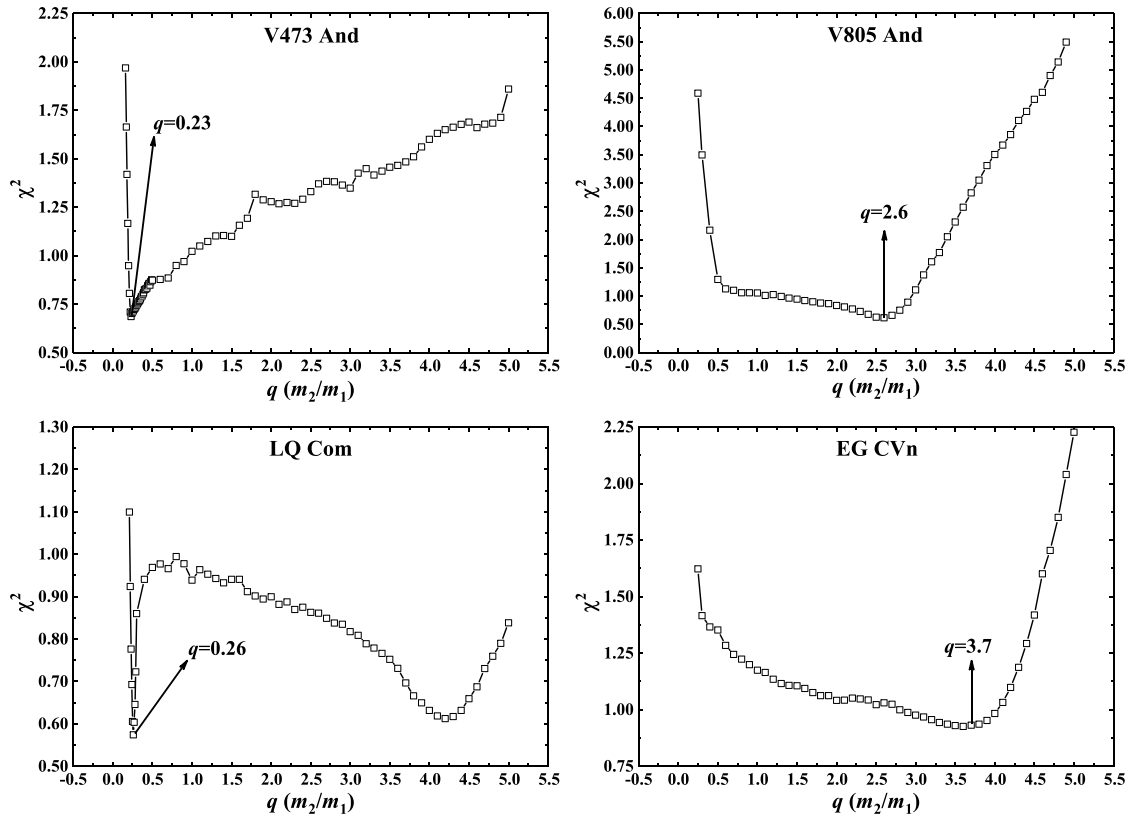
Figure 2. Relations between χ^2 and mass ratio q of four targets: V473 And, V805 And, LQ Com, and EG CVn.

solutions. The final solutions of these four targets are listed in Table 4 and the corresponding theoretical light curves are displayed in Figure 1 as solid lines. The theoretical light curves could well fit the observation data for V473 And, but slightly deviate from the observational ones around the out-of-eclipse maxima for V805 And, LQ Com, and EG CVn.

It is well known that many W UMa-type contact binaries show asymmetries in two out-of-eclipse maxima of their light curves, which is known as the O'Connell effect (O'Connell 1951). Usually, it is very difficult to identify the slight asymmetry (i.e., the weak O'Connell effect) by a visual inspection. In order to justify weather the light curves of our four targets are symmetrical, or not, we employed two measurements to quantify their possible asymmetries in their light curves. The simplest and conventional measurement is the magnitude difference (Δm_{max}) between two out-of-eclipse maxima

$$\Delta m_{max} = m_{max.II} - m_{max.I}. \qquad (2)$$

Another one, called the O'Connell Effect Ratio (OER), was proposed by McCartney (1997). It is the ratio of the areas beneath the two maxima of a phased light curve. In the numerical scheme, one may first divide the phased light curve into n equally wide bins, where n is chosen to sufficiently sample the light curve. Then, the weighted mean magnitude in each bin is calculated and normalised by subtracting the mean magnitude in the bin including the primary minimum. The OER is finally calculated according to the definition

$$OER = \frac{\sum_{k=1}^{n/2}(m_k - m_1)}{\sum_{k=n/2+1}^{n}(m_k - m_1)}, \qquad (3)$$

where m_k represents the weighted mean magnitude in the kth bin. Obviously, OER can more thoroughly detect the asymmetries of a light curve than Δm_{max}. If $\Delta m_{max} > 0$ or $OER > 1$, the O'Connell effect is positive, or it will be negative.

In view of the high precision of TESS photometry, the wideband (approximately 600–1000 nm) and long-cadence (30 min) observations of three targets are also used to estimate the possible O'Connell effect and derive photometric solutions. The data product of TESS includes the Single Aperture Photometry (SAP) and the Pre-search Data Conditioning light curves. The latter has been processed to make it more suitable for detecting shallow transits of extrasolar planets, and not intended for eclipse binaries which show large variability amplitudes. Thus, we adopted only the SAP data in the present work. The SAP flux data are downloaded from Mikulski Archive for Space Telescopes (MAST) portal[k] and converted into magnitude units. We excluded the data points with a nonzero flag for the QUALITY parameter.

Table 5 summarised both Δm and OER of the light curve of each band for all four targets. From Table 5, we can conclude that the light curves of V473 And, obtained from both our observations and TESS photometry, are almost perfect symmetrical, while there are slight asymmetries (i.e., weak O'Connell effects) for the other three targets. It should be noted that although both two measurements for the ground-based observations of LQ Com, suggest the existence of positive O'Connell effect, we cannot decide it because the values of Δm_{max} are close and even smaller to the corresponding mean errors. But fortunately, the observation dates of TESS for

Table 4. Photometric solutions of four contact binaries.

Parameter	V473 And	V805 And	LQ Com	EG CVn
i(degree)	75.82(15)	83.40(14)	86.25(51)	77.20(14)
$g_1 = g_2$	0.32	0.32	0.32	0.32
$A_1 = A_2$	0.5	0.5	0.5	0.5
$\Omega_1 = \Omega_2$	2.259(3)	5.903(7)	2.358(3)	7.363(10)
T_1(K)	6381	5467	6404	6304
T_2(K)	6266(6)	5350(3)	6178(11)	6230(7)
$q = m_2/m_1$	0.239(1)	2.568(6)	0.263(2)	3.755(9)
$\frac{L1}{L_1+L_2}$ (B)	0.7917(13)	0.3277(7)	0.8027(18)	0.2507(13)
$\frac{L1}{L_1+L_2}$ (V)	0.7888(12)	0.3225(6)	0.7945(15)	0.2484(11)
$\frac{L1}{L_1+L_2}$ (R)	0.7866(12)	0.3186(5)	0.7899(14)	0.2467(9)
r1 (pole)	0.4885(4)	0.2907(2)	0.4740(5)	0.2676(3)
r1 (side)	0.5335(6)	0.3046(3)	0.5134(7)	0.2808(4)
r1 (back)	0.5625(7)	0.3454(4)	0.5395(7)	0.3281(9)
r2 (pole)	0.2635(16)	0.4462(7)	0.2523(21)	0.4796(7)
r2 (side)	0.2770(20)	0.4794(9)	0.2629(25)	0.5217(10)
r2 (back)	0.3291(48)	0.5102(13)	0.2974(46)	0.5511(14)
$f = \frac{\Omega_{in}-\Omega}{\Omega_{in}-\Omega_{out}}$	45.1(4.8)%	22.0(3.1)%	15.1(5.3)%	37.6(4.8)%
χ^2	0.6843	0.6074	0.5645	0.9197

Table 5. Measurements of O'Connell effects for the four targets.

Target	Band[a]	Median HJD	Δm_{max}	OER	Error[b]
V473 And	GB-B	2458086	−0.0088	0.9931	0.0086
	GB-V	2458086	0.0024	0.9968	0.0081
	GB-R	2458086	0.0104	1.0228	0.0115
	TESS-W	2458780	0.0013	0.9983	0.0082
V805 And	GB-B	2459163	0.0219	1.0213	0.0134
	GB-V	2459163	0.0121	1.0198	0.0117
	GB-R	2459163	0.0117	1.0193	0.0106
LQ Com	GB-B	2458966	0.0218	1.0251	0.0215
	GB-V	2458966	0.0105	1.0292	0.0168
	GB-R	2458966	0.0058	1.0168	0.0156
	TESS-W	2458912	0.0143	1.0270	0.0094
EG CVn	GB-B	2457141	−0.0128	0.9695	0.0091
	GB-V	2457141	−0.0113	0.9740	0.0084
	GB-R	2457141	−0.0130	0.9776	0.0092
	TESS-W	2458940	−0.0104	0.9765	0.0081

[a]In this column, GB-B, V and R denote the ground-based observation with B, V and R band, respectively. TESS-W refers to the wide-band observations of TESS.
[b]The errors are the mean error of the corresponding photometric data.

LQ Com were just very close to those of our ground-based observations. Moreover, TESS light curve suggests a significant and the same positive O'Connell effect as our ground-based observations. Thus, we come to the conclusion that there exists a positive O'Connell effect for LQ Com.

In general, the O'Connell effect could be interpreted as a result of the spots on the surface of the component stars. According to the above calculations, the light curves of both V805 And and LQ Com show a positive O'Connell effect, while the light curves of EG CVn presented a weak and negative O'Connell effect. The positive/negative O'Connell effect could be caused by any one of the following four spot models: (1) a hot spot on the primary star (HS1); (2) a cool spot on the primary star (CS1); (3) a hot spot on the secondary star (HS2); (4) a cool spot on the secondary star (CS2). With the four different spot models, we reapplied the W−D code to fit the photometric data and obtained the photometric solutions with different spot models, which are compiled in Table 6. Among those spot models, the model with a cool spot on the primary component (CS1) seems to be the optimal one to reproduce the observational light curves for V805 And, LQ Com and EG CVn, because its chi-square value is smallest. However, it should be noted that the differences of χ^2 among four different spot models are rather negligible for the three targets, especially for V805 And and EG CVn.

In order to determine the optimal solutions, we also fitted the TESS light curves with each of those spot models using the W−D code. During the analyses of TESS light curves, the photometric solutions without spot derived from our ground-based observations are set as the initial parameters. The limb darkening coefficients for TESS light curves were taken from Claret (2017). The corresponding photometric solutions are summarised in Table 7. Although χ^2 of four different spot models did not also significantly deviate from each other, the optimal light-curves solutions tended to the CS1. The results are consistent with those derived from our ground-based observations. Thus, we think that the CS1 is the optimal one among the four possible spot models for there three targets. The theoretical light curves corresponding to the optimal photometric solutions for both TESS and our ground-based observations, were calculated and showed as the solid lines in Figure 3.

Because the O'Connell effect is positive for V805 And and LQ Com, but be negative for EG CVn, the cool spots for V805 And and LQ Com could be observed around phase 0.25, while the cool spot for EG CVn could be around phase 0.75 (see the three upper panels of Figure 4). In addition, except from the spot's parameters, these photometric solutions with different spot models did not significantly deviate from each other. Thus, we would adopt the photometric solutions of CS1 for both V805 And, LQ Com, and EG CVn in the following analysis.

According to the photometric solutions, the orbital inclinations for V805 And and LQ Com are larger than 80°, confirming the total-eclipse inference from their light-curves morphology. For V473 And and EG CVn, the photometric solutions suggest that they are the partial-eclipse binaries, but very close to the total eclipse. The total- or partial-eclipse characteristics for the four targets could be checked visually from the geometrical configurations shown in the bottom panels of Figure 4. In addition, we noted that in the photometric solutions with different spot models, the primary components of both V805 And and EG CVn have lower masses and higher temperatures than their secondary components, implying that they are two W-subtype contact binaries.

Although the radial-velocity curves for the four binaries are absent so far, we can still estimate their absolute physical parameters according to the following two different methods: (1) the scheme based on the *Gaia* distance (Kjurkchieva et al. 2019), and (2) the empirical relations (Qian 2003; Gazeas 2009; Yu et al. 2022). The standard procedure for the former was proposed by Kjurkchieva et al. (2019) and developed by Liu et al. (2020) and Li et al. (2021). In our calculations, the V-band magnitudes V_{ASASSN} at maximum brightness were determined from the

Table 6. Photometric solutions with spot for V805 And, LQ Com and EG CVn derived from our ground-based observations.

Parameter	V805 And				LQ Com				EG CVn			
Spot model	HS1	CS1	HS2	CS2	HS1	CS1	HS2	CS2	HS1	CS1	HS2	CS2
i(deg)	83.04(3)	83.71(13)	83.09(10)	83.65(13)	85.31(34)	86.01(40)	85.32(34)	85.72(51)	77.11(13)	77.17(13)	77.14(13)	77.44(13)
$g_1 = g_2$	0.32	0.32	0.32	0.32	0.32	0.32	0.32	0.32	0.32	0.32	0.32	0.32
$A_1 = A_2$	0.5	0.5	0.5	0.5	0.5	0.5	0.5	0.5	0.5	0.5	0.5	0.5
$\Omega_1 = \Omega_2$	5.930(7)	5.855(2)	5.938(7)	5.824(3)	2.354(3)	2.380(4)	2.354(3)	2.342(3)	7.265(10)	7.378(10)	7.250(4)	7.430(8)
T_1(K)	5467	5467	5467	5467	6404	6404	6404	6404	6304	6304	6304	6304
T_2(K)	5358(2)	5348(2)	5358(2)	5352(2)	6264(17)	6264(9)	6180(9)	6158(11)	6282(8)	6193(7)	6284(7)	6196(6)
$q = m_2/m_1$	2.581(5)	2.540(1)	2.587(5)	2.517(1)	0.260(1)	0.269(1)	0.260(1)	0.258(1)	3.677(8)	3.768(8)	3.669(2)	3.809(7)
$\frac{L1}{L_1+L_2}$ (B)	0.3244(7)	0.3312(6)	0.3240(6)	0.3319(6)	0.7917(28)	0.7882(15)	0.8040(16)	0.8068(18)	0.2458(13)	0.2561(12)	0.2461(11)	0.2539(11)
$\frac{L1}{L_1+L_2}$ (V)	0.3196(6)	0.3259(5)	0.3192(5)	0.3267(5)	0.7866(21)	0.7829(12)	0.7959(13)	0.7980(15)	0.2451(10)	0.2527(9)	0.2454(9)	0.2506(9)
$\frac{L1}{L_1+L_2}$ (R)	0.3160(6)	0.3218(4)	0.3155(4)	0.3228(4)	0.7836(18)	0.7801(11)	0.7914(12)	0.7930(14)	0.2446(9)	0.2502(8)	0.2450(8)	0.2482(7)
r1 (pole)	0.2897(2)	0.2930(2)	0.2897(2)	0.2937(2)	0.4730(5)	0.4678(6)	0.4734(5)	0.4778(5)	0.2695(3)	0.2672(3)	0.2684(3)	0.2665(3)
r1 (side)	0.3034(3)	0.3072(2)	0.3034(2)	0.3079(2)	0.5121(6)	0.5052(8)	0.5125(7)	0.5184(7)	0.2827(4)	0.2804(4)	0.2814(4)	0.2796(4)
r1 (back)	0.3435(4)	0.3490(4)	0.3435(4)	0.3497(4)	0.5381(7)	0.5307(8)	0.5383(8)	0.5447(8)	0.3299(8)	0.3278(7)	0.3269(8)	0.3270(7)
r2 (pole)	0.4448(6)	0.4448(2)	0.4445(6)	0.4440(2)	0.2550(17)	0.2571(20)	0.2528(19)	0.2494(16)	0.4762(7)	0.4808(7)	0.4757(3)	0.4814(6)
r2 (side)	0.4774(9)	0.4776(3)	0.4770(9)	0.4766(3)	0.2660(20)	0.2681(24)	0.2635(23)	0.2597(19)	0.5172(11)	0.5233(10)	0.5165(4)	0.5241(8)
r2 (back)	0.5076(12)	0.5084(3)	0.5070(12)	0.5076(4)	0.3023(38)	0.3038(44)	0.2985(42)	0.2936(35)	0.5462(14)	0.5529(13)	0.5455(5)	0.5536(11)
$f = \frac{\Omega_{in}-\Omega}{\Omega_{in}-\Omega_{out}}$	20.5(2.7)%	23.7(0.7)%	20.5(2.7)%	23.7(0.8)%	13.5(3.6)%	9.9(4.0)%	13.5(3.6)%	18.1(3.7)%	37.3(4.4)%	37.8(4.5)%	38.0(1.4)%	37.9(3.8)%
Co-Latitude(deg)	99.6(3.4)	94.5(1.6)	76.0(2.4)	102.9(4.0)	99.8(5.6)	82.0(1.3)	70.5(3.9)	101.4(8.3)	60.2(5.0)	86.8(4.5)	87.4(9.5)	104.6(2.1)
Longitude(deg)	264.2(1.6)	98.6(1.5)	87.4(1.7)	272.2(1.4)	227.9(3.7)	7.0(0.5)	53.1(3.2)	309.2(5.0)	128.5(4.4)	235.6(3.3)	320.5(3.4)	61.0(3.5)
Radius(deg)	10.5(0.2)	14.0(0.2)	7.7(0.1)	9.3(0.2)	14.8(0.4)	14.3(0.2)	12.7(0.4)	16.2(1.4)	14.6(0.4)	15.7(0.4)	9.3(0.3)	12.7(0.5)
$T_{\rm s}/T_{\rm ph}$	1.19(0.01)	0.82(0.01)	1.16(0.01)	0.78(0.01)	1.08(0.01)	0.75(0.01)	1.27(0.02)	0.84(0.03)	1.13(0.01)	0.84(0.01)	1.11(0.02)	0.91(0.01)
χ^2	0.4531	0.4465	0.4534	0.4472	0.3998	0.3133	0.4098	0.5553	0.6814	0.6488	0.6620	0.6554

Table 7. Photometric solutions without/with spot for V473 And, LQ Com and EG CVn obtained from TESS's observations.

| Paramete	V473 And	LQ Com					EG CVn				
Spot model	WS	WS	HS1	CS1	HS2	CS2	WS	HS1	CS1	HS2	CS2
i(deg)	77.19(10)	85.86(19)	85.33(23)	85.59(25)	85.16(25)	85.70(15)	77.27(16)	77.33(16)	77.07(18)	77.42(16)	76.84(14)
$g_1 = g_2$	0.32	0.32	0.32	0.32	0.32	0.32	0.32	0.32	0.32	0.32	0.32
$A_1 = A_2$	0.5	0.5	0.5	0.5	0.5	0.5	0.5	0.5	0.5	0.5	0.5
$\Omega_1 = \Omega_2$	2.206(1)	2.362(3)	2.346(2)	2.363(2)	2.335(2)	2.356(2)	7.246(16)	7.272(15)	7.320(11)	7.256(15)	7.264(9)
T_1(K)	6381	6404	6404	6404	6y404	6404	6304	6304	6304	6304	6304
T_2(K)	6269(4)	6165(8)	6267(13)	6229(8)	6192(7)	6147(8)	6245(7)	6276(8)	6178(9)	6285(8)	6179(7)
$q = m_2/m_1$	0.222(1)	0.278(1)	0.271(1)	0.279(1)	0.266(1)	0.280(1)	3.760(13)	3.781(12)	3.816(7)	3.767(12)	3.772(6)
$\frac{L1}{L_1+L_2}$ (W)	0.7941(6)	0.7787(8)	0.7728(15)	0.7723(6)	0.7822(7)	0.7779(7)	0.2507(9)	0.2464(9)	0.2554(11)	0.2461(9)	0.2572(9)
r1 (pole)	0.4980(3)	0.4768(4)	0.4781(3)	0.4753(3)	0.4797(3)	0.4756(3)	0.2762(5)	0.2760(4)	0.2747(4)	0.2763(4)	0.2757(4)
r1 (side)	0.5466(4)	0.5180(6)	0.5196(4)	0.5159(4)	0.5217(4)	0.5163(4)	0.2913(6)	0.2910(5)	0.2896(5)	0.2913(5)	0.2907(5)
r1 (back)	0.5764(5)	0.5473(7)	0.5482(4)	0.5447(5)	0.5505(5)	0.5450(5)	0.3508(14)	0.3503(12)	0.3486(13)	0.3506(12)	0.3498(12)
r2 (pole)	0.2616(9)	0.2650(13)	0.2620(11)	0.2648(12)	0.2620(11)	0.2654(10)	0.4858(12)	0.4847(11)	0.4865(7)	0.4843(11)	0.4863(6)
r2 (side)	0.2755(12)	0.2774(16)	0.2741(13)	0.2771(15)	0.2742(13)	0.2779(12)	0.5306(18)	0.5291(16)	0.5316(11)	0.5285(16)	0.5314(10)
r2 (back)	0.3341(32)	0.3194(32)	0.3154(26)	0.3189(30)	0.3165(27)	0.3206(24)	0.5626(24)	0.5606(22)	0.5633(15)	0.5600(22)	0.5635(13)
$f = \frac{\Omega_{in}-\Omega}{\Omega_{in}-\Omega_{out}}$	57.2(4.1)%	31.6(3.7)%	32.5(3.3)%	32.2(3.2)%	32.8(3.4)%	37.4(3.3)%	57.2(8.2)%	57.3(7.6)%	56.8(4.8)%	57.0(7.6)%	56.8(4.0)%
Co-Latitude(deg)	–	–	100.3(3.8)	99.5(2.6)	70.3(5.6)	121.9(6.1)	–	95.8(5.4)	89.8(6.1)	85.1(10.5)	77.0(3.8)
Longitude(deg)	–	–	231.5(2.9)	17.3(2.3)	55.4(2.7)	258.4(10.9)	–	120.2(4.4)	219.1(4.4)	299.4(4.7)	40.7(5.4)
Radius(deg)	–	–	15.0(0.3)	14.9(0.5)	12.8(0.3)	13.3(0.6)	–	14.6(0.5)	15.4(0.4)	9.2(0.3)	11.9(0.4)
T_s/T_{ph}	–	–	1.10(0.01)	0.87(0.01)	1.36(0.01)	0.82(0.02)	–	1.15(0.01)	0.81(0.01)	1.12(0.01)	0.91(0.01)
χ^2	0.4408	0.8338	0.4715	0.4176	0.4879	0.5377	0.6869	0.5286	0.4565	0.5229	0.4636
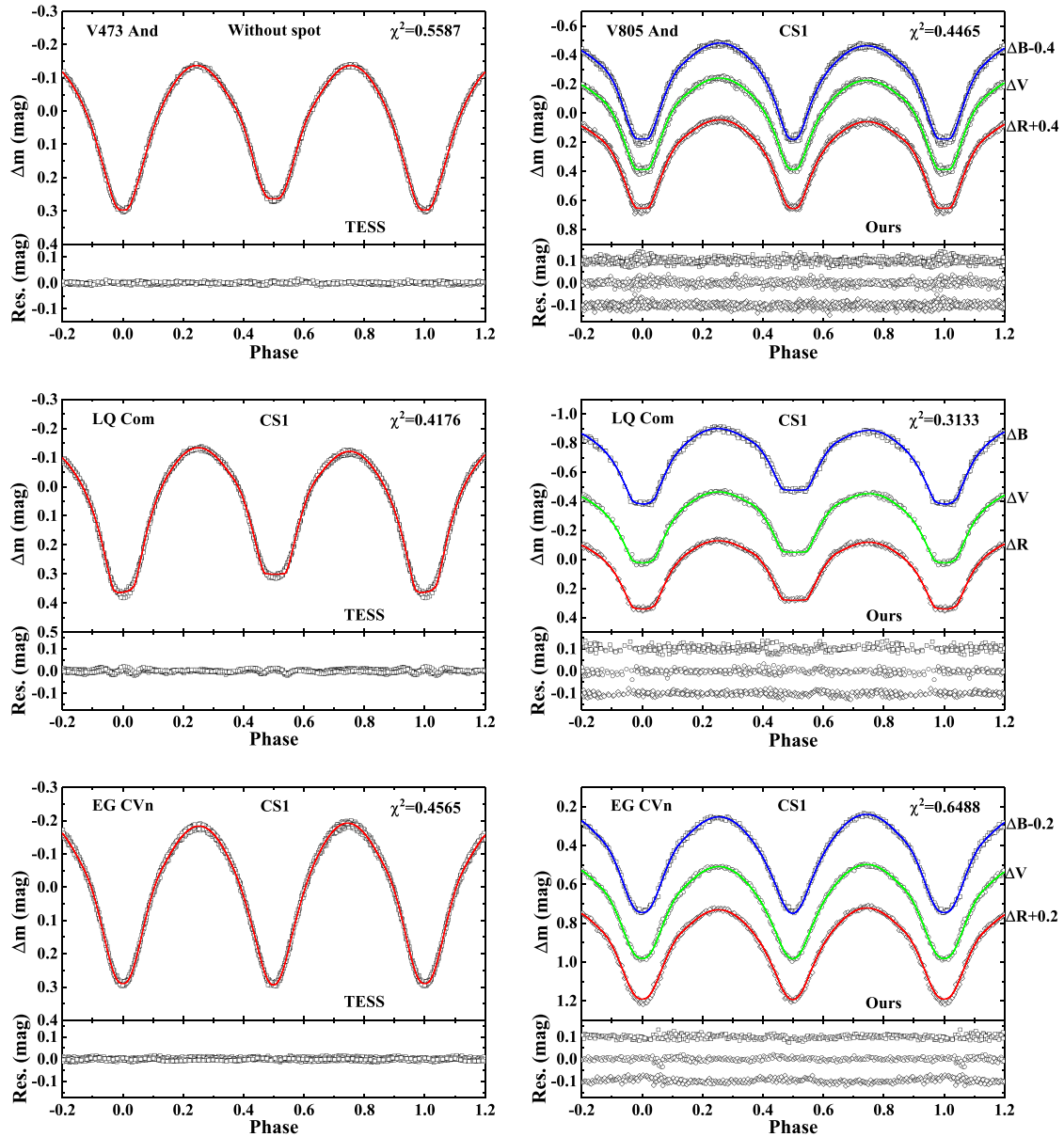
Figure 3. Observed (symbols) light curves from TESS (left panels) and our ground-based observations (right panels). Theoretical light curves corresponding to their respective optimal solutions are plotted as solid lines. Bottom of each panel: the corresponding residuals (the residuals for *B* and *R* bands are vertically shifted by 0.1 and –0.1 mag, respectively).

phase-folded light curves of ASAS-SN observations, the interstellar extinctions A_V were derived with the S&F method (Schlafly & Finkbeiner 2011) from the IRAS database.[1] The bolometric corrections BC_V were interpolated from the calibration proposed by Pecaut & Mamajek (2013). These parameters are summarised in Table 8. For the later, we adopted the up-date empirical relation between the semi-major axis and orbital period derived by Yu et al. (2022),

$$\log a = 0.856(18) \log P + 0.784(7). \qquad (4)$$

Combining our photometric solutions with the semi-major axis determined from the two distinct methods, we calculated the

absolute parameters of the four targets which are summarised in Table 9. For V473 And, LQ Com, and EG CVn, two sets of parameters calculated from two distinct methods are almost equal within the error range. However for V805 And, the absolute parameters calculated from the *Gaia* distance are significantly deviated from those determined from the empirical relation. As has been pointed out by Li et al. (2021), the absolute parameters for most of the contact binaries (more than 80% of contact binaries) can be well estimated from the *Gaia* distance. But for a friction of contact binaries, the absolute parameters determined from the *Gaia* distance may be unreliable and even unrealistic due to many reasons, such as too far away, the third-light effect, inaccurate interstellar extinction, and inaccurate *V*-band magnitude at maximum brightness. Therefore, in the following analysis, we adopted the weighted mean parameters for V473 And, LQ Com, and EG CVn, and the parameters determined by the empirical relation for V805 And.

[1]https://irsa.ipac.caltech.edu/applications/DUST/.

Table 8. *Gaia* distances, *V*-band magnitudes at maximum brightness, interstellar extinctions, bolometric corrections, Absolute *V*-band magnitude, and absolute bolometric magnitudes of Four Target Binaries.

Target	Distance(pc)	V_{ASASSN}	A_V	m_V	M_V	BC_V	M_{bol}
V473 And	1182.0(22.4)	13.565(0.022)	0.0004(0.0001)	13.565(0.022)	3.202(0.064)	−0.050(0.001)	3.152(0.065)
V805 And	1543.2(69.1)	14.703(0.048)	0.0003(0.0001)	14.703(0.048)	3.761(0.143)	−0.170(0.003)	3.591(0.146)
LQ Com	606.4(15.1)	12.554(0.037)	0.0400(0.0012)	12.514(0.038)	3.600(0.092)	−0.050(0.001)	3.550(0.093)
EG CVn	672.5(5.9)	12.821(0.026)	0.0216(0.0031)	12.780(0.030)	3.662(0.048)	−0.060(0.001)	3.602(0.049)

The values in parentheses represent the standard error which are calculated according to the error propagation rule.

Table 9. Absolute physical parameters of four target binaries calculated from two different methods and their corresponding weighted means.

Target	Method	$a(R_\odot)$	$M_1(M_\odot)$	$M_2(M_\odot)$	$R_1(R_\odot)$	$R_2(R_\odot)$	$L_1(L_\odot)$	$L_2(L_\odot)$
	GD	2.863(0.087)	1.577(0.145)	0.377(0.036)	1.510(0.048)	0.826(0.033)	3.409(0.228)	0.949(0.079)
V473 And	ER	2.783(0.091)	1.448(0.143)	0.346(0.036)	1.468(0.049)	0.803(0.034)	3.221(0.229)	0.897(0.078)
	WM	2.825(0.063)	1.512(0.102)	0.362(0.025)	1.489(0.034)	0.815(0.024)	3.315(0.133)	0.923(0.056)
	GD	3.426(0.227)	0.773(0.154)	1.963(0.392)	1.081(0.073)	1.632(0.110)	0.942(0.128)	1.965(0.266)
V805 And	ER	3.035(0.093)	0.537(0.050)	1.363(0.127)	0.958(0.030)	1.445(0.045)	0.739(0.048)	1.541(0.099)
	WM	3.091(0.086)	0.560(0.048)	1.420(0.121)	0.976(0.028)	1.471(0.042)	0.764(0.045)	1.593(0.093)
	GD	2.493(0.111)	1.285(0.172)	0.346(0.048)	1.248(0.057)	0.687(0.038)	2.364(0.230)	0.656(0.076)
LQ Com	ER	2.517(0.087)	1.323(0.139)	0.356(0.039)	1.260(0.045)	0.694(0.031)	2.409(0.188)	0.669(0.064)
	WM	2.508(0.068)	1.308(0.108)	0.352(0.030)	1.255(0.035)	0.691(0.024)	2.391(0.146)	0.664(0.049)
	GD	2.458(0.058)	0.342(0.025)	1.289(0.095)	0.714(0.018)	1.273(0.032)	0.727(0.040)	2.152(0.119)
EG CVn	ER	2.471(0.087)	0.348(0.037)	1.310(0.143)	0.723(0.027)	1.268(0.050)	0.746(0.059)	2.133(0.179)
	WM	2.462(0.048)	0.344(0.021)	1.295(0.079)	0.717(0.015)	1.272(0.027)	0.733(0.033)	2.146(0.099)

The values in parentheses represent the standard error which are calculated according to the error propagation rule.
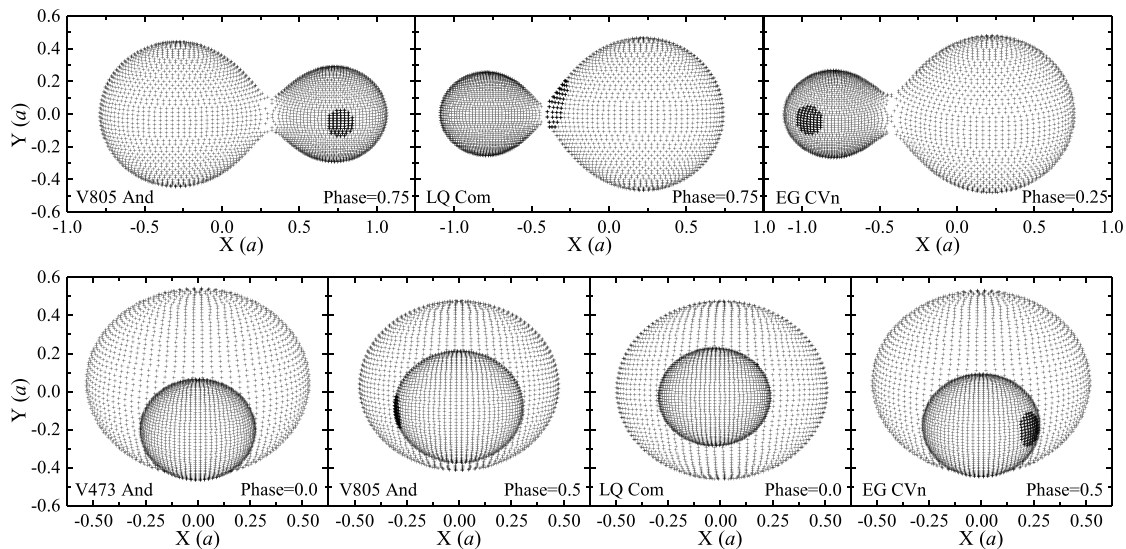
Figure 4. Upper three panels display the geometrical configurations of V805 And and EG CVn for the best photometric solutions with one spot. Bottom four panels display the geometrical configurations of four binary systems at phase 0.0 or 0.5 for visually checking whether are they the total-eclipse contact binaries or not.

4. Orbital period variations and their physical origins

4.1. Orbital period variations

The orbital period variations of close binaries have an underlying implication to various astrophysical processes and dynamical evolution of binary systems. In order to uncover the period variation of the four targets: V473 And, V805 And, LQ Com, and EG

CVn, we performed an extensive search for all available eclipse timings, and obtained 107 data points from the literature and the eclipse timings database (i.e., the O-C gateway[m]). From our observations, we calculated 16 eclipse timings with the K-W method (Kwee & van Woerden 1956). In addition, from several surveys

[m]http://var.astro.cz/ocgate/.

(e.g., NSVS, WASP, and ASAS-SN, ZTF, TESS, etc.), we extracted the photometric data of the four targets and calculated the phase-folded light curves. With the method of Borkovits et al. (2015), we derived 114 eclipse timings. Finally, a total of 237 eclipse timings, including those collected from the literature and calculated from our observations and surveys' ones, are compiled in Table 10.

In order to build the $O - C$ diagrams, we constructed the following linear ephemerides

$$\text{Min.I} = T_0 + P_0 \times E, \qquad (5)$$

where T_0 is the primary eclipse timing derived from our observations and P_0 is the orbital period determined by Jayasinghe et al. (2018). With the linear ephemerides, we calculated the $O - C$ values for their eclipse timings which are displayed in Figure 5. Clearly, the $O - C$ diagrams for V473 And, V805 And, and EG CVn, exhibit a complex variation. However, the variation of the $O - C$ curve for LQ Com seems to be not observable due to the large scatters. In order to uncover the secular period changes, we first adopt the quadratic function, i.e.,

$$O - C = \Delta T_0 + \Delta P_0 \times E + \gamma E^2, \qquad (6)$$

to fit their $O - C$ values. Among the four targets, LQ Com should be not undergoing a secular period variation because the coefficient of its quadratic term is 3 orders of magnitude smaller than the typical values for contact binaries (Hu et al. 2018). Thus, for LQ Com, we adopted a linear fit. After subtracting the linear or quadratic fit, the residuals $(O - C)_1$ still exhibit the obvious periodic variation. By introducing the sinusoidal term into the quadratic function, i.e.,

$$O - C = \Delta T_0 + \Delta P_0 \times E + \gamma E^2 + A \sin(\omega E + \phi), \qquad (7)$$

we can achieve the sufficiently good fits.

By assigning the reciprocals of the normalised square errors as the weights and using the weighted least-squares method, we derived the fitting parameters which were summarised in Table 11. As should be mentioned, although the errors for two eclipse timings of V805 And are absent, we performed a weighted fit by cutting the two data points. The quadratic term implied that V473 and, V805 And and EG CVn are undergoing a secular period change. The sinusoidal term revealed a cyclic Eclipse-Timing Variation (ETV) for all four targets. Based on the fitting parameters, we calculated the rates of secular period changes and the modulation periods of cyclic ETVs (see the third and fourth lines from the bottom of Table 11).

4.2. Physical origins of orbital period variations

4.2.1. Secular period changes

The above orbital period investigations suggested that V473 And, V805 And, and EG CVn shows the secular orbital period decrease and increase, respectively. The secular orbital period variations could be, in general, interpreted as a result of the mass transfer and/or the mass and angular momentum loss. According to the photometric solutions, these three binaries are not in the relatively deep contact configuration ($f < 50\%$), i.e., their surface potentials are significantly lower than those of their outer Lagrange points. Thus, it should be difficult and even impossible to loss their mass via Roche-lobe overflow from the outer Lagrange point. In addition, the typical mass-loss rate due to stellar wind for an active dwarf star is about 10^{-10} $M_\odot \cdot yr^{-1}$ (Mullan et al. 1992) or even

lower (Lim & White 1996). It contributes the decrease rate of orbital period at the level of $\sim 10^{-10}$ $d \cdot yr^{-1}$, which is two or three orders of magnitude smaller than the observed ones (typical observed value is 10^{-7} $d \cdot yr^{-1}$, Hu et al. 2018). Thus, the effect of mass loss on orbital period decrease may be neglected for V473 And, V805 And, and EG CVn.

When considering the mass conservation and the circular orbit of a contact binary, its orbit evolution can be dominated by

$$\frac{\dot{J}}{J} = \frac{\dot{P}}{3P} + \dot{M}_1 \left(\frac{1}{M_1} - \frac{1}{M_2} \right), \qquad (8)$$

where $J = \sqrt[3]{\frac{G^2 M_1 M_2 P}{2\pi(M_1 + M_2)}}$ is the orbital angular momentum. Equation (6) suggests explicitly that both the conservative mass transfer and the angular momentum loss could yield the secular period changes.

In regard of the angular momentum loss, the most plausible mechanism is the magnetic breaking due to stellar wind. From the standard magnetic breaking model (Weber & Davis 1967), Guinan & Bradstreet (1988) derived the period decrease rate caused by the angular momentum loss via magnetic stellar wind

$$\dot{P}_{aml} \approx -1.1 \times 10^{-8} \cdot \frac{(1 + q)^2}{q} \cdot \frac{k^2 \left(M_1 R_1^4 + M_2 R_2^4 \right)}{(M_1 + M_2)^{5/3} P^{7/3}}. \qquad (9)$$

In the formula, the gyration constant k^2 is roughly 0.1 estimated from the main sequence stars. By putting the absolute physical parameters into Equation (7), we estimated the orbital period decrease rates of -1.59×10^{-7} $d \cdot yr^{-1}$, -7.92×10^{-8} $d \cdot yr^{-1}$ and -1.18×10^{-7} $d \cdot yr^{-1}$ for V473 And, V805 And and EG CVn, respectively. For V473 And and V805 And, the orbital period decrease rates due to the angular momentum loss are smaller than the observed values, implying the angular momentum loss via magnetic stellar wind could not fully yield the observed orbital period decrease. For EG CVn, the orbital period is undergoing a secular increase at the rate of 2.69×10^{-7} $d \cdot yr^{-1}$, but the angular momentum loss due to magnetic stellar wind can only lead to secular orbital period decrease. Thus, in order to yield the observed orbital period increase/decrease for V473 And, V805 And, and EG CVn, the conservative mass transfer seems to be required.

Combining Equation (8) with (9), we may write the mass-transfer rate as

$$\dot{M}_1 = -\dot{M}_2 = \frac{M_1 M_2}{3P(M_1 - M_2)} \cdot (\dot{P}_{obs} - \dot{P}_{aml}), \qquad (10)$$

where $\dot{P}_{obs} - \dot{P}_{aml}$ denotes the secular orbital period variation yielded by the conservative mass transfer. Thus, if the secular orbital period changes of V805 And and EG CVn are yielded by a combination of the angular momentum loss and the mass transfer, the conservative mass transfer rates would be $\dot{M}_2 = -\dot{M}_1 = 5.89 \times 10^{-9}$ $M_\odot \cdot yr^{-1}$ for V473 And, $\dot{M}_1 = -\dot{M}_2 = 2.58 \times 10^{-7}$ $M_\odot \cdot yr^{-1}$ for V805 And, and $\dot{M}_2 = -\dot{M}_1 = 1.73 \times 10^{-7}$ $M_\odot \cdot yr^{-1}$ for EG CVn. If the secular orbital period changes are caused separately by the conservative mass transfer (i.e., $\dot{P}_{aml} = 0$), the required mass transfer rates are $\dot{M}_2 = 6.86 \times 10^{-8}$ $M_\odot \cdot yr^{-1}$ for V473 And, $\dot{M}_1 = 3.11 \times 10^{-7}$ $M_\odot \cdot yr^{-1}$ for V805 And, and $\dot{M}_2 = 1.20 \times 10^{-7}$ $M_\odot \cdot yr^{-1}$ for EG CVn. We may estimate the ranges of mass-transfer rate as $[0.59 \sim 6.86] \times 10^{-8}$ $M_\odot \cdot yr^{-1}$, $[2.58 \sim 3.11] \times 10^{-7}$ $M_\odot \cdot yr^{-1}$ and $[1.20 \sim 1.73] \times 10^{-7}$ $M_\odot \cdot yr^{-1}$ for V805 And and EG CVn, respectively.

According to the thermal timescale of the donor star ($\tau_{th} \sim \frac{GM_{donor}^2}{R_{donor} L_{donor}}$, Paczyński 1971) of V473 And, V805 And and EG CVn,

Table 10. Eclipse Timings of four targets collected from literature and calculated from our observations or surveys' data.

Target	HJD	Error	Type	Ref.	HJD	Error	Type	Ref.	HJD	Error	Type	Ref.
V473 And	2451424.29000[a]	0.00314	s	1	2451424.49233[a]	0.00303	p	1	2451442.75624	0.00309	s	2
	2454378.47006[b]	0.00022	p	1	2454378.67150[b]	0.00025	s	1	2455836.3902	0.0006	p	3
	2455837.3928	0.0010	s	3	2455837.5932	0.0013	p	3	2455843.4114	0.0008	s	3
	2455843.6124	0.0008	p	3	2455846.4217	0.0012	p	3	2455878.5260	0.0011	p	3
	2456185.5181	0.0004	p	4	2456186.3198	0.0007	p	4	2456254.7403	0.0006	s	5
	2456520.4017	0.0021	s	6	2456520.6031	0.0005	p	6	2456553.3065	0.0010	s	4
	2456644.4018	0.0015	s	4	2456917.48445[c]	0.00199	p	1	2456917.68302[c]	0.00252	s	1
	2457281.05704[c]	0.00189	p	1	2457281.26004[c]	0.00198	s	1	2457646.23981[c]	0.00108	p	1
	2457646.43911[c]	0.00106	s	1	2457727.09970[d]	0.00015	s	1	2457728.10446[d]	0.00007	p	1
	2458019.04380[c]	0.00158	p	1	2458019.24544[c]	0.00159	s	1	2458087.06515[d]	0.00010	s	1
	2458088.06890[d]	0.00010	p	1	2458353.52590[c]	0.00181	s	1	2458353.72949[c]	0.00180	p	1
	2458399.07482[e]	0.00383	p	1	2458399.27628[e]	0.00036	s	1	2458402.28611[e]	0.00034	p	1
	2458402.48629[e]	0.00031	s	1	2458753.42252[e]	0.00041	p	1	2458753.62259[e]	0.00041	s	1
	2458769.47373[e]	0.00038	p	1	2458769.67420[e]	0.00032	s	1	2458769.87528[f]	0.00047	p	1
	2458770.07603[f]	0.00021	s	1	2458783.51949[f]	0.00018	p	1	2458783.72015[e]	0.00019	s	1
	2459139.87322[e]	0.00038	p	1	2459140.07367[e]	0.00029	s	1	2459173.58274[e]	0.00036	p	1
	2459173.78253[e]	0.00034	s	1	–	–	–	–	–	–	–	–
V805 And	2453223.73863[b]	0.00101	p	1	2453223.96322[b]	0.00119	s	1	2454377.33046[b]	0.00011	s	1
	2454377.55432[b]	0.00010	p	1	2456155.52605	0.00090	p	7	2456249.193	–	p	8
	2456854.0790	–	s	9	2456898.46764	0.00026	s	7	2456904.68425[c]	0.00030	s	1
	2456904.90828[c]	0.00063	p	1	2456930.43403	0.00033	s	7	2456987.2580	0.0010	s	10
	2457309.33806[c]	0.00034	p	1	2457309.55991[c]	0.00029	s	1	2457693.5701	0.0003	s	10
	2457694.4580	0.0005	s	10	2457694.6789	0.0001	p	10	2457733.3034	0.0009	p	10
	2457748.3962	0.0005	p	10	2457759.4964	0.0003	p	10	2458009.6535	0.0006	s	10
	2458017.6456	0.0011	s	10	2458029.6349	0.0016	s	10	2458042.5068	0.0004	s	10
	2458078.4650	0.0007	s	10	2458080.4629	0.0006	p	10	2458112.4271	0.0017	p	10
	2458122.41362[c]	0.00042	s	1	2458122.63423[c]	0.00036	p	1	2458124.4130	0.0008	p	10
	2458381.6747	0.0035	s	10	2458384.5594	0.0035	p	10	2458384.7804	0.0035	s	10
	2458434.5018	0.0035	s	10	2458447.15374[d]	0.00007	p	1	2458448.04173[d]	0.00006	p	1
	2458448.26400[d]	0.00007	s	1	2458794.75453[e]	0.00042	p	1	2458794.97591[e]	0.00046	s	1
	2458837.14981[d]	0.00005	s	1	2459110.83383[e]	0.00042	p	1	2459111.05541[e]	0.00038	s	1
	2459111.50132[g]	0.00029	s	1	2459164.10656[d]	0.00006	p	1	2459165.21654[d]	0.00009	s	1
	2459166.10472[d]	0.00006	s	1	–	–	–	–	–	–	–	–
LQ Com	2451260.8579	0.0009	p	11	2451288.8760	0.0050	s	11	2453060.0220	0.0033	p	12
	2453115.69031[g]	0.00454	p	1	2453115.86476[g]	0.00341	s	1	2453178.13532[b]	0.00017	p	1
	2453178.31286[b]	0.00021	s	1	2453623.28467[g]	0.00307	s	1	2453623.46407[h]	0.00213	p	1
	2453842.20566[b]	0.0003	p	1	2453842.38259[b]	0.00035	s	1	2454133.9190	0.0001	s	13
	2454164.78411[b]	0.00014	p	1	2454164.96236[b]	0.00013	s	1	2454912.35351	0.00200	p	14
	2454925.37832	0.00200	s	14	2454933.4060	0.0006	p	15	2454933.5853	0.0011	s	15
	2454937.5099	0.0009	s	15	2455304.33563	0.00010	s	14	2455310.4057	0.0048	s	16
	2455310.5815	0.0011	p	16	2455315.40085	0.00160	s	14	2455651.35870	0.00100	p	17
	2455662.4213	0.0008	p	18	2455662.6003	0.0017	s	18	2455674.37538	0.00020	s	17
	2455674.55205	0.00160	p	17	2455675.4468	0.0014	s	18	2455687.39846	0.00030	p	17
	2455959.66308	0.00020	p	17	2456008.3722	0.0018	s	19	2456008.5497	0.0004	p	19
	2456074.38695	0.00040	s	17	2456400.35338	0.00045	p	20	2456428.36744	0.00021	s	20
	2456723.46870	0.00040	s	21	2456747.55448[c]	0.00299	p	1	2456747.73498[c]	0.00538	s	1
	2456786.44875	0.00020	p	21	2457090.11486[c]	0.00200	p	1	2457090.29484[c]	0.00082	s	1

Table 10. Continued.

Target	HJD	Error	Type	Ref.	HJD	Error	Type	Ref.	HJD	Error	Type	Ref.
	2457100.4660	0.0010	p	22	2457100.6413	0.0018	s	22	2457117.41528	0.00070	s	23
	2457125.44212	0.00030	p	23	2457461.93753[c]	0.00054	p	1	2457462.11559[c]	0.00066	s	1
	2457465.5017	0.0049	p	24	2457483.34940	0.00080	p	23	2457817.70074[c]	0.00045	p	1
	2457817.88034[c]	0.00049	s	1	2457852.3162	0.0004	p	25	2457852.4966	0.0015	s	25
	2457892.45844[i]	0.00059	s	1	2457892.64328[i]	0.00238	p	1	2457901.38394[g]	0.00043	s	1
	2458217.35933[g]	0.00044	p	1	2458226.4580	0.0021	s	10	2458245.37284[g]	0.00020	s	1
	2458540.4752	0.0012	s	26	2458907.12293[f]	0.00013	p	1	2458907.30262[f]	0.00013	s	1
	2458921.75370[f]	0.00015	p	1	2458921.93280[f]	0.00013	p	1	2458956.36616[g]	0.00025	p	1
	2458956.54590[g]	0.00026	s	1	2458966.17994[d]	0.00006	s	1	2459303.20920[d]	0.00014	p	1
	2459323.19768[d]	0.00013	p	1	–	–	–	–	–	–	–	–
EG CVn	2451259.7031	0.0006	s	27	2451310.8766	0.0018	p	27	2451363.26914[a]	0.00148	p	1
	2451363.43734[a]	0.00195	s	1	2451573.35281[a]	0.00123	s	1	2451573.52662[a]	0.00115	p	1
	2452001.7327	0.0002	p	28	2452285.5102	0.0012	s	27	2452285.6886	0.0004	p	27
	2452287.6107	0.0006	s	27	2452296.5182	0.0011	p	27	2452296.6901	0.0008	s	27
	2452308.5659	0.0005	s	27	2452308.7351	0.0021	p	27	2452344.3681	0.0007	p	27
	2452344.5409	0.0006	s	27	2452347.3352	0.0003	s	27	2452691.5461	0.0006	p	29
	2453045.3600	0.0040	p	30	2453045.5332	0.0007	s	30	2453188.91169[b]	0.00021	p	1
	2453189.08548[b]	0.00024	s	1	2453463.44010	0.00074	p	31	2453788.4428	0.0006	s	32
	2453864.58440[b]	0.00032	s	1	2453864.75888[b]	0.00029	p	1	2454172.4727	0.0005	p	33
	2454191.15981[b]	0.00017	s	1	2454191.33448[b]	0.00018	p	1	2454538.8661	0.0002	p	34
	2454889.8873	0.0008	p	35	2455000.4356	0.0006	s	35	2455398.4390	0.0006	p	36
	2455643.45534	0.00010	s	14	2455957.62992	0.00010	p	14	2456670.67907	0.00030	s	21
	2456748.39273[c]	0.00073	p	1	2456748.56725[c]	0.00090	s	1	2457111.46360[c]	0.00088	s	1
	2457111.63838[c]	0.00089	p	1	2457141.15383[d]	0.00025	s	1	2457141.32948[d]	0.00026	p	1
	2457153.37961	0.00030	s	23	2457180.44694	0.00050	p	23	2457465.45803	0.00030	p	23
	2457471.91572[c]	0.00089	s	1	2457472.09139[c]	0.00073	p	1	2457836.03782[c]	0.00061	p	1
	2457836.21028[c]	0.00150	s	1	2457901.52584[g]	0.00050	s	1	2457902.40331[g]	0.00034	p	1
	2458195.7931	0.0002	p	37	2458276.30130[e]	0.00091	s	1	2458276.47538[e]	0.00043	p	1
	2458281.88903[e]	0.00050	s	1	2458282.06330[e]	0.00069	p	1	2458586.45761[e]	0.00057	s	1
	2458586.63272[e]	0.00037	p	1	2458593.44330[e]	0.00049	s	1	2458593.61749[e]	0.00057	p	1
	2458922.46183[e]	0.00035	s	1	2458922.63677[e]	0.00055	p	1	2458935.38460[f]	0.00014	s	1
	2458935.56003[f]	0.00015	p	1	2458941.49708[g]	0.00034	p	1	2458950.57895[f]	0.00010	p	1
	2458950.75313[f]	0.00013	s	1	2459250.08268[e]	0.00109	s	1	2459250.25937[e]	0.00162	p	1
	2459250.95734[e]	0.00130	p	1	2459251.13042[e]	0.00142	s	1	2459680.39030[g]	0.00012	s	1

References: 1. This paper; 2. Kuzmin (2008); 3. Banfi et al. (2012); 4. Corfini et al. (2014); 5. Diethelm (2013); 6. Hubscher (2014); 7. (Vrastak 2015); 8. Yao et al. (2015); 9. GCVS; 10. Paschke (2019); 11. Diethelm (2001); 12. Paczyński et al. (2006); 13. Nelson (2008); 14. Brat et al. (2011); 15. Hubscher et al. (2010); 16. Hubscher & Monninger (2011); 17. Hoňková et al. (2013); 18. Hubscher, Lehmann, & Walter (2012); 19. Hubscher et al. (2013); 20. Honková et al. (2014); 21. Honkova et al. (2015); 22. Hubscher (2016); 23. Jurýšek et al. (2017); 24. Hubscher (2017); 25. Pagel (2018); 26. Pagel (2020); 27. Blattler & Diethelm (2002); 28. Nelson (2002); 29. Diethelm (2003); 30. Diethelm (2004); 31. Diethelm (2005); 32. Diethelm (2006); 33. Diethelm (2007); 34. Nelson (2009); 35. Diethelm (2009); 36. Diethelm (2011); 37. Nelson (2019).
[a] These times were derived from the photometric data of NSVS.
[b] These times were derived from the photometric data of WASP.
[c] These times were derived from the photometric data of ASAS-SN.
[d] These times were derived from our observations.
[e] These times were derived from the photometric data of ZTF.
[f] These times were derived from the photometric data of TESS.
[g] These times were derived from the photometric data of BRNO.
[h] These times were derived from the photometric data of ASAS DR3.
[i] These times were derived from the photometric data of AAVSO.

we estimated the mass transfer rates on the thermal timescale $\frac{M_{donor}}{\tau_{th}} = -1.05 \times 10^{-8}$ $M_\odot \cdot yr^{-1}$, -5.23×10^{-8} $M_\odot \cdot yr^{-1}$ and 4.89×10^{-8} $M_\odot \cdot yr^{-1}$. For V473 and, the mass transfer rate on the thermal timescale is significantly larger than the upper limit of the mass transfer rate estimated from Equation (10), implying that its

secular period decrease should be involved with some additional mechanisms, e.g., the mass/angular momentum loss and unstable mass transfer. For V805 And and EG CVn, the thermal-timescale mass transfer rates are significantly smaller than the lower limits of the mass transfer rates determined from Equation (10), implying
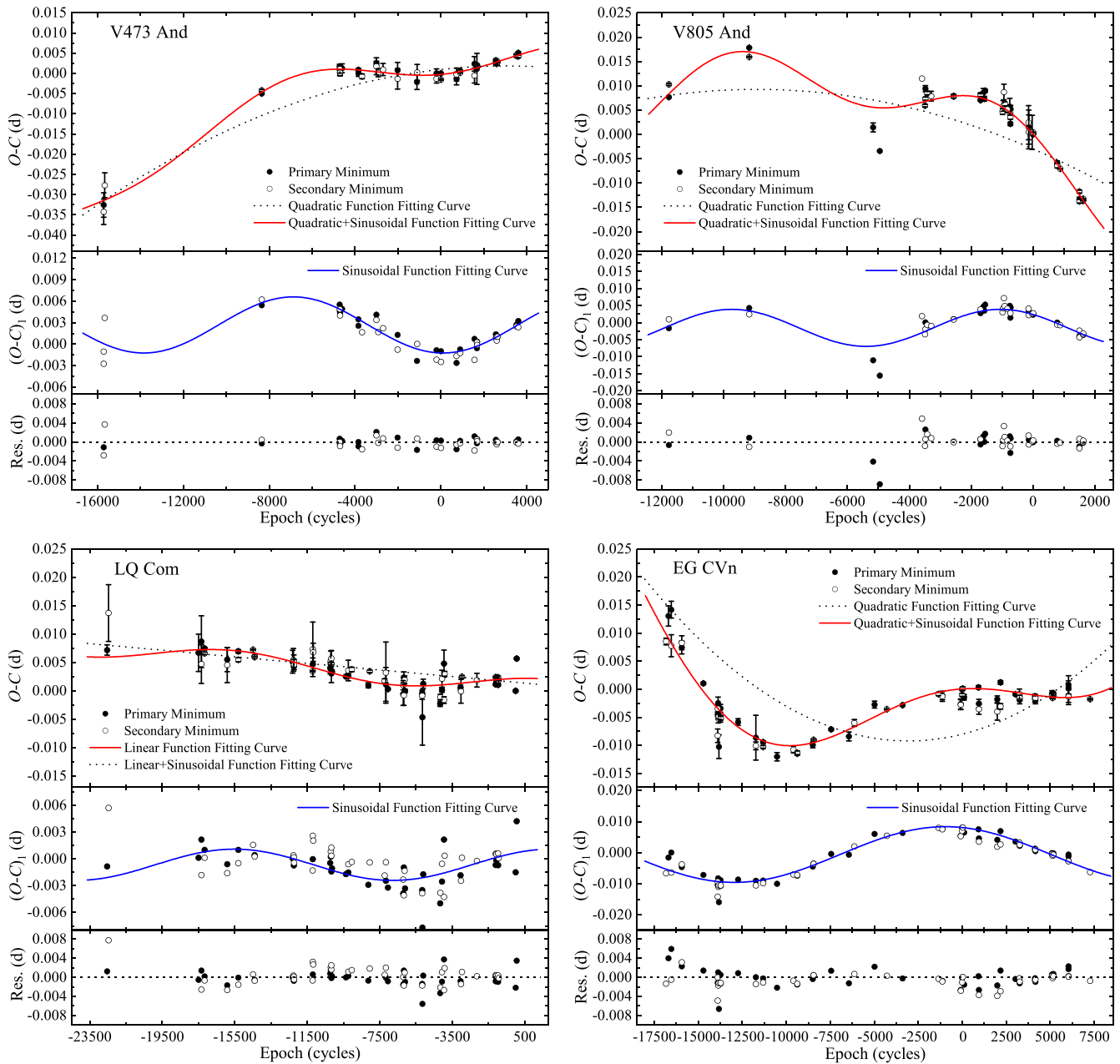
Figure 5. $O-C$ diagrams (symbols) and fitting curves (dotted or solid lines) for four targets: V473 And (upper left), V805 And (upper right), LQ Com (left bottom), and EG CVn (right bottom). Top of each panel: $O-C$ curves and the fitting curves of the linear/quadratic function (dotted line) and the linear/quadratic function superimposed a sinusoidal term (solid line). Middle: residuals $(O-C)_1$ (symbols) after subtracting the linear/quadratic fit and the fitting curve of the sinusoidal function (solid line). Bottom: the final residuals.

that the conservative mass transfer could yield the observed period decrease and increase.

Theoretically, the continuous mass transfer could yield the impacting spots on the surface of the mass gaining component (Flannery 1975; Zhou & Leung 1990; Zhai & Fang 1995; Zhu et al. 2009; Hu et al. 2019). For V805 And, the more massive secondary is slightly cooler than the primary. Moreover, due to the contact configuration, the surface potentials of two components are equal so that there is not accreting energy to heat the transferred material. Thus, the spot yielded by mass transfer should be a cool one. Under the effect of Coriolis force, this cool spot can move to a small longitude and be observed around phase 0.75. These

theoretical predictions seem to be just consistent with the best photometric solutions (CS1), indicating that the cool spot might be indeed yielded by the mass transfer. However, for EG CVn, the optimal photometric solution (CS1) cannot match the theoretical prediction of impacting spot, which means that the cool spot of EG CVn may be originated from the magnetic activity of its primary component.

4.2.2. Cyclic period changes

The above analyses of $O-C$ curves suggested that all four targets: V473 And, V805 And, LQ Com, and EG CVn, show periodic

Table 11. Linear ephemerides and fitting parameters of $O - C$ curves for the four binaries: V473 And, V805 And, LQ Com and EG CVn.

Name	V473 And	V805 And	LQ Com	EG CVn	Unit
T_0	2457728.10446	2458447.15374	2459303.20920	2457141.32948	day
P_0	0.4012974	0.4439421	0.3568355	0.3492761	day
ΔT_0	$3.66(0.28) \times 10^{-3}$	$-3.85(0.19) \times 10^{-3}$	$0.84(0.17) \times 10^{-3}$	$-8.63(0.33) \times 10^{-3}$	day
ΔP_0	$0.57(0.10) \times 10^{-6}$	$-4.33(0.16) \times 10^{-6}$	$-0.29(0.03) \times 10^{-6}$	$0.79(0.08) \times 10^{-6}$	day
γ	$-0.95(0.18) \times 10^{-10}$	$-2.84(0.14) \times 10^{-10}$	–	$1.28(0.09) \times 10^{-10}$	day
A	$3.92(0.30) \times 10^{-3}$	$5.43(0.39) \times 10^{-3}$	$1.75(0.33) \times 10^{-3}$	$8.95(0.47) \times 10^{-3}$	day
ω	$2.58(0.29) \times 10^{-2}$	$4.15(0.38) \times 10^{-2}$	$2.06(0.20) \times 10^{-2}$	$1.50(0.15) \times 10^{-2}$	deg$\cdot P^{-1}$
ϕ	267.62(5.60)	133.65(4.15)	49.98(10.99)	104.28(3.47)	deg
$\dot{P}_{\mathrm{obs}}$	$-1.73(0.32) \times 10^{-7}$	$-4.67(0.23) \times 10^{-7}$	–	$2.69(0.19) \times 10^{-7}$	day$\cdot$yr^{-1}
P_{mod}	15.31(1.72)	10.55(0.97)	17.06(1.65)	22.95(2.32)	yr
$\sum_i (O_i - C_i)^2$	0.517×10^{-4}	0.663×10^{-4}	2.426×10^{-4}	2.548×10^{-4}	–
χ^2	3.106	3.445	22.750	8.400	–

ETVs. The periodic ETVs are, generally, regarded as the cyclic period variation of an eclipsing binary. However, for some cases, they are not the embodiment of the cyclic period variations. This is dependent on the causes yielding the cyclic ETVs. So far, there are at least three different causes of cyclic ETVs: (1) the apsidal motion; (2) the light-time effect due to the third body; (3) the cyclic magnetic activity. For the cyclic ETVs of the three targets, we can exclude the apsidal motion because the primary and secondary eclipse timings do not follow a reversed-phase variation. Thus, we would focus on the light-time effect due to a third body and the cyclic magnetic activity.

4.2.2.1. Light-time effect due to third body. If the cyclic ETVs of V473 And, V805 And, LQ Com, and EG CVn, are caused by the light-time effect of the third body (Irwin 1952), the orbits of their third body should be or at least close to circular one because of the good sinusoidal fits for the $O - C$ curves. By inserting the modulation period P_{mod} and amplitude A of cyclic ETVs into the following equation

$$f(M_3) = \frac{4\pi^2}{G P_{\mathrm{mod}}^2} \cdot (a_{12} \sin i')^3, \quad (11)$$

where $a_{12} \sin i' = A \times c$ (a_{12} and i' denote the orbital radius and inclination of eclipse binary pair or third body around the barycentre of triple system, and c is light velocity), we may determine the mass function $f(M_3)$ of the third body. Based on the equation

$$f(M_3) = \frac{M_3^3 \sin^3 i'}{(M_1 + M_2 + M_3)^3}, \quad (12)$$

we could then obtain the relation between the mass M_3 and orbital inclination i' of the third body. Figure 6 shows the relations between the mass and orbital inclination of the third bodies for these four targets. If these third bodies move just in a coplanar orbit around their corresponding host binaries, their masses are equal to 0.184, 0.336, 0.066 and 307 M$_\odot$, respectively. When $i' = 90°$, the third bodies of four binary systems would reach their minimum masses, i.e., 0.178, 0.334, 0.066 and 0.298 M$_\odot$, respectively. For LQ Com, the minimum mass is about 70 times of mass of Jupiter. If there really exists the third body orbiting LQ Com, it should be a brown dwarf. For V473 And, V805 And, and EG CVn, the minimum masses of third bodies are comparable to those of

the less massive components of their hosting binaries. Their third bodies might be a stellar companion. Thus, it can be expected to detect the spectra and light contributions of the third bodies. Unfortunately, the spectroscopic observations for these targets are absent so far. For the light contributions of the third bodies, our photometric studies did not suggest any significant third lights. Of course, it should be very difficult, or even unrealistic to detect the third light from light curves.

The most direct way to confirm the existence of the third body orbiting a binary system is to detect the transiting circumbinary events (Carter et al. 2011; Zhang, Qian, & He 2017a; Socia et al. 2020) of the third body from the photometric light curves with high resolution, or the radial-velocity change of binary system (i.e., the so-called γ-velocity variation, Van Hamme & Wilson 2007). However, the transiting circumbinary events are very rare because of both strict limitation to the orbital geometry and the low frequency of occurrence. For the γ-velocity variation, as has been mentioned, the spectroscopic observations for these targets are still absent. In addition, the gravitational interaction of the third body may typically result in precession of orbital plane of binary system, which could be observable as a change of eclipsing depth on a long timescale. But for our targets, both the low-precision observations from early surveys and the disturbances of magnetic activity spots did not allow us to precisely detect any significant eclipse-depth variations on a long timescale. Of course, besides the Røemer delay (the light-time effect), the third body may also yield the dynamical delay on eclipse timings (Soderhjelm 1975; Borkovits et al. 2003, 2011, 2015, 2016). Because of the short orbital periods ($P < 1$ d) of the targeting binaries and the relatively long modulation periods ($P_{\mathrm{mod}} \sim 10$ yr) of the third bodies, the classical Røemer delay will dominate the ETVs and the dynamical delay may be negligible (Rappaport et al. 2013). In view of these facts, the follow-up spectroscopic and photometric observations for these binaries should be performed to confirm the existence of their third bodies.

4.2.2.2. Cyclic magnetic activity. Regarding the explanation of the cyclic magnetic activity, Applegate (1992) proposed a theoretical model to explain the cyclic period oscillations for contact binaries. It has been developed lately by Lanza, Rodono, & Rosner (1998) and Lanza & Rodonò (2002). According to this theory, strong magnetic activities below the surface of one or
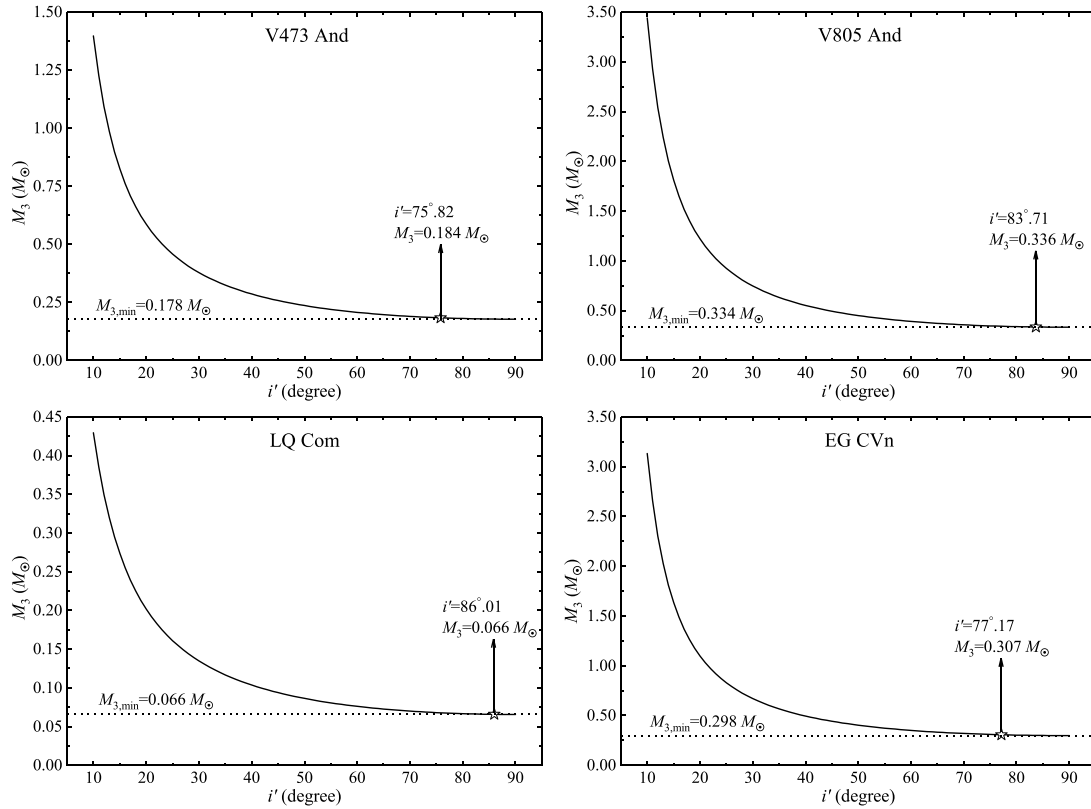
Figure 6. Relations between the mass and orbital inclination of the third body for V473 And (upper left), V805 And (upper right), LQ Com (left bottom), and EG CVn (right bottom).

both components play major roles in producing the cyclic period variations. When the magnetic field distribution of an active component changes during its magnetic cycle, the distribution of angular momentum will be also adjusted. This sequentially yields variations of the quadrupole moment, resulting in variations of the star's oblateness and radial differential rotation. Variations in shape of the star would be gravitationally coupled to the orbit, modulating the orbital period. Meanwhile, the luminosity of the active component would be variable with variations of its shape.

Using the modulation period and amplitude of cyclic period variation, we may firstly calculate the amplitude ΔP and relative amplitude $\Delta P/P$ of orbital period modulation with the formula

$$\Delta P = 2\pi A \frac{P}{P_{\mathrm{mod}}}. \tag{13}$$

The other model parameters, i.e., the change of quadruple moment ΔQ, the transferred angular momentum ΔJ, the relative variation of angular velocity $\Delta \Omega / \Omega$, the required energy ΔE, the relative luminosity change $\Delta L/L$, and the required strength of magnetic field B, can be obtained from the following formulas derived by Applegate (1992)

$$\Delta Q = \frac{1}{9} \mathrm{M} a^2 \frac{\Delta P}{P}, \tag{14}$$

$$\Delta J = \frac{GM^2}{R} \left(\frac{a}{R}\right)^2 \frac{\Delta P}{6\pi}, \tag{15}$$

$$\frac{\Delta \Omega}{\Omega} = \frac{M}{M_{\mathrm{shell}}} \frac{GM}{3R^3} \left(\frac{a}{R}\right)^2 \left(\frac{P}{2\pi}\right)^2 \frac{\Delta P}{P}, \tag{16}$$

$$\Delta E = 2 \frac{(\Delta J)^2}{I_{\mathrm{shell}}}, \tag{17}$$

$$\frac{\Delta L}{L} = \pi \frac{\Delta E}{P_{\mathrm{mod}} L}, \tag{18}$$

$$B^2 \sim 10 \frac{GM^2}{R^4} \left(\frac{a}{R}\right)^2 \frac{\Delta P}{P_{\mathrm{mod}}}. \tag{19}$$

In these formulas, G is the gravitational constant, M_{shell} and I_{shell} denote the mass and the moment of inertia of the shell for the active component, respectively. M, R, and L are the mass, radius, and luminosity of the active component.

By insetting the absolute physical parameters and modulation period of three targets into the above formulas, we calculated the model parameters needed to yield the observed cyclic period variations for the three targets, which are listed in Table 12. In the calculations, the mass of convective shell was assumed to be typically equal to one-tenth of the mass of the corresponding active component, i.e., $M_{\mathrm{shell}} = 0.1 M_{\mathrm{active}}$. Also, our calculations were performed for both the primary and secondary components because both two components of these binaries can, in principle, satisfy the condition to yield strong magnetic field. In addition, the typical values of those model parameters required by Applegate's mechanism are presented in the penultimate column of Table 12 for a reference. Clearly, our four binaries are observed to undergo orbital period modulation with amplitude $\Delta P/P \sim 10^{-6}$, over time scales of $P_{\mathrm{mod}} \sim 10$ yr. These modulations can be yielded by

Table 12. Model parameters for magnetic activity of three binaries: V473 And, V805 And, LQ Com, and EG CVn.

Name	V473 And		V805 And		Typical value	Unit
Component	Primary	Secondary	Primary	Secondary		
ΔP	$1.77(0.34) \times 10^{-6}$		$3.93(0.64) \times 10^{-6}$		$10^{-5} \sim 10^{-6}$	day
$\Delta P/P$	$4.40(0.84) \times 10^{-6}$		$8.86(1.45) \times 10^{-6}$		$10^{-5} \sim 10^{-6}$	–
ΔQ	$5.69(1.34) \times 10^{49}$	$1.36(0.32) \times 10^{49}$	$4.69(1.06) \times 10^{49}$	$1.19(0.27) \times 10^{50}$	10^{49}	g·cm^2
ΔJ	$1.70(0.40) \times 10^{47}$	$5.93(1.39) \times 10^{46}$	$2.06(0.46) \times 10^{47}$	$3.88(0.87) \times 10^{47}$	$10^{46} \sim 10^{47}$	g·cm$^2 \cdot$ s^{-1}
$\Delta\Omega/\Omega$	$2.90(0.68) \times 10^{-4}$	$1.41(0.33) \times 10^{-3}$	$2.65(0.60) \times 10^{-3}$	$8.62(1.94) \times 10^{-4}$	~ 0.01	–
ΔE	$2.67(1.26) \times 10^{40}$	$4.56(2.14) \times 10^{40}$	$2.69(1.21) \times 10^{41}$	$1.64(0.74) \times 10^{41}$		erg
$\Delta L/L$	$1.37(0.67) \times 10^{-2}$	$8.37(4.13) \times 10^{-2}$	$8.96(3.76) \times 10^{-1}$	$2.62(1.10) \times 10^{-1}$	~ 0.1	–
B	$2.44(0.42) \times 10^{3}$	$3.56(0.62) \times 10^{3}$	$6.27(0.99) \times 10^{3}$	$4.64(0.74) \times 10^{3}$	$10^{3} \sim 10^{4}$	G
Name	LQ Com		EG CVn		Typical value	Unit
Component	Primary	Secondary	Primary	Secondary		
ΔP	$0.63(0.18) \times 10^{-6}$		$2.34(0.36) \times 10^{-6}$		$10^{-5} \sim 10^{-6}$	day
$\Delta P/P$	$1.76(0.50) \times 10^{-6}$		$6.71(1.03) \times 10^{-6}$		$10^{-5} \sim 10^{-6}$	–
ΔQ	$1.55(0.53) \times 10^{49}$	$4.18(1.42) \times 10^{48}$	$1.50(0.29) \times 10^{49}$	$5.64(1.09) \times 10^{49}$	10^{49}	g·cm^2
ΔJ	$5.95(2.02) \times 10^{46}$	$2.58(0.88) \times 10^{46}$	$7.92(1.53) \times 10^{46}$	$2.01(0.39) \times 10^{47}$	$10^{46} \sim 10^{47}$	g·cm$^2 \cdot$ s^{-1}
$\Delta\Omega/\Omega$	$1.47(0.50) \times 10^{-4}$	$7.81(2.65) \times 10^{-4}$	$2.23(0.43) \times 10^{-3}$	$4.78(0.92) \times 10^{-4}$	~ 0.01	–
ΔE	$5.34(3.63) \times 10^{39}$	$1.23(0.84) \times 10^{40}$	$1.10(0.43) \times 10^{41}$	$6.00(2.32) \times 10^{40}$		erg
$\Delta L/L$	$3.40(2.27) \times 10^{-3}$	$2.83(1.89) \times 10^{-2}$	$1.75(0.72) \times 10^{1}$	$3.24(1.32) \times 10^{-2}$	~ 0.1	–
B	$1.77(0.39) \times 10^{3}$	$2.85(0.62) \times 10^{3}$	$4.07(0.60) \times 10^{3}$	$2.74(0.40) \times 10^{3}$	$10^{3} \sim 10^{4}$	G

the gravitational coupling of the orbit to variations in the shape of a magnetically active component in these systems. In order to yield the variable deformation of their active stars, the distribution of angular momentum needed to be variable at a level of $\Delta J \sim 10^{47}$ g·cm$^2 \cdot$ s^{-1}, to produce the variation of the quadrupole moment at a level of $\Delta Q \sim 10^{49}$ g·cm^2. Meanwhile, due to the variation of shape of the active component, the relative luminosity variation should be at the $\Delta L/L \simeq 0.01$ level, and the active component would be differentially rotating at the $\Delta\Omega/\Omega \simeq 0.01$ level. The torque needed to redistribute the angular momentum should be exerted by a mean subsurface magnetic field of several kilogauss. Obviously, the variations of those model parameters and the mean subsurface magnetic field, well followed the typical values required by Applegate's mechanism. These results indicated that the cyclic period changes for all four targets may be interpreted as a result of the cyclic magnetic activity.

For the energy required by Applegate's model, Brinkworth et al. (2006) proposed another quantised criterion, i.e., whether the active component can provide enough energy to support Applegate's mechanism, or not. According to the method of Brinkworth et al. (2006), we calculated the available energies[n] generated by the components for the four targets. Because the energy required by Applegate's mechanism is very sensitive to the assumed shell mass, the required energies with various different shell masses are calculated and showed in Figure 7. From Figure 7, it can be seen that except for the less massive primary components of V805 And, the available energies provided by the components for all four targets may significantly exceed the required ones for a certain range of shell mass, i.e., these components can generate

enough energy to drive Applegate's mechanism. In another word, the observed cyclic period variations for the four targets may be caused by the cyclic magnetic activity of at least one component of these binaries. Of course, some observable evidences should be further investigated to confirm the explanation of cyclic magnetic activity. For instance, the luminosity variation and any other indicator of magnetic activity (starspot activity, coronal X-ray luminosity, emission cores in CaII or MgII lines, etc.) should also show the same period as the orbital period modulation (Kim et al. 1997; Hu et al. 2020). However, these evidences require a long-term (the timescale of several decades, or at least one period of cyclic period variation) photometric and/or spectroscopic observations.

5. Evolution of contact binaries

Based on the absolute physical parameters, we located the four binaries at the mass-radius and mass-luminosity diagrams (Figure 8) to discuss their evolutionary states. For comparison, 179 contact binaries collected by Yu et al. (2022) were also added in Figure 8. In the diagrams, the Zero-Age Main Sequence (ZAMS) and Terminal-Age Main Sequence (TAMS) lines were calculated based on the PARSEC models[o] (Bressan et al. 2012). All the contact binaries are classified into two subtypes: A and W subtype. Similar to other contact binaries, the more massive components of our four targets are mainly located on the main sequence band and fairly close to the ZAMS line with relatively high metallicity. The less massive components exhibit the over-sized and over-luminous characteristics relative to the single star with the same mass. They have radii 3-4 times larger than expected for the corresponding ZAMS masses. Both Lucy (1968) and Moses (1976) suggested the

---

[n]In our calculations, the radial mass density of the active component was derived from the Lane-Emden equation by assuming the polytropic exponent of $n = 1.5$ as an approximation to the full convective star.
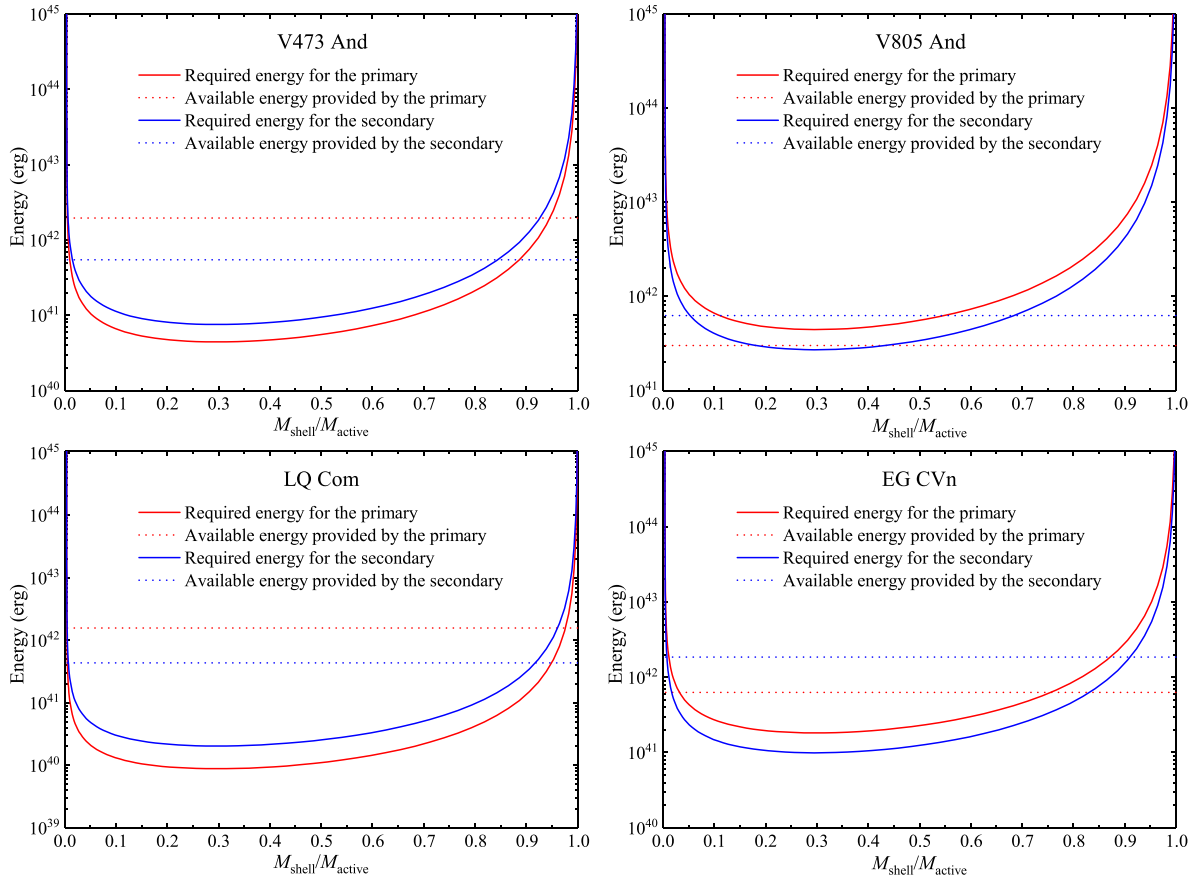
[o]http://stev.oapd.inaf.it/cgi-bin/cmd.

Figure 7. Required energy for the primary (red solid line) and secondary (blue solid line) of V473 And (upper left), V805 And (upper right), LQ Com (left bottom), and EG CVn (right bottom) as a function of mass ratio between shell mass and total mass of the active star. The dashed lines represent the available energies provided by their primary (red dotted line) and secondary (blue dotted line).

over-size and over-luminous phenomena for the less massive components are caused by the energy transfer from the more massive component to the less massive one. However, it seems physically hard to inflate a ZAMS star to such size purely by the energy transfer from its more massive companion (Stępień 2004). So, the less massive components should be more evolved with hydrogen depleted in their centres.

Although both A- and W-subtype systems belong to the same family of low-mass contact binaries, the evolutionary relation between two subtypes is still a matter of controversy and debate. Following the original idea of Lucy (1976), Hilditch King & McFarlane (1988) and Hilditch (1989) suggested that the A-subtype contact binaries are more evolved than the W-subtype systems from the mass-radius and colour-luminosity diagrams. However, by further analysing the mass-luminosity and period-angular momentum diagrams, both Maceroni & van't Veer (1996) and Yakut & Eggleton (2005) pointed out that the conclusion of Hilditch et al. (1988) might be incorrect. Moreover, from a statistical standpoint, because the total mass and angular momentum of A-subtype systems are significantly larger than those of W-subtype systems, the A-subtype contact binaries should be less evolved than the W-subtype (Gazeas & Niarchos 2006).

Combining the catalog of Yu et al. (2022) with our four targets, we here systematically calculated the statistical averages of physical parameters for two subtypes of contact binaries (Table 13). Clearly,

the W-subtype contact binaries have shorter orbital periods and lower temperatures than the A-subtype systems. The two statistical features are similar with those of Rucinski (1974) and Smith (1984), indicating that the W-subtype systems are more evolved than A-subtype ones. Moreover, similar to the statistical results of Gazeas & Niarchos (2006), our calculations also show that both the total mass and orbital angular momentum of W-subtype systems are lower than those of A-subtype ones. In addition, we found that the temperature difference between two components of a W-subtype system is significantly smaller than that of an A-subtype one, implying that W-subtype systems should be closer to the thermal equilibrium state than A-subtype systems. These statistical evidences show formation of W-subtype systems from A-subtype systems is possible, but the opposite direction is not strongly supported. Usually, the evolution from A-subtype to W-subtype systems may be accompanied by a simultaneous mass and angular momentum loss, as well as mass and energy exchanges between two components of a contact binary. Thus, the opposite evolutionary direction seems to be impossible, because it requires an increase of both total mass, orbital angular momentum, and temperature difference.

An additional evidence for the evolutionary direction is that binary systems with shorter orbital periods are, in general, kinematically older (age 8 Gyr) than those with longer periods (age 2 Gyr) (Bilir et al. 2005). Of course, there is an alternative

Table 13. Statistical averages of physical parameters for two subtypes of contact binaries.

Subtype	Period	a	M_1	M_2	R_1	R_2	L_1	L_2	T_1	T_2	ΔT	M_{tot}	J_{orb}
A	0.50263	3.352	1.568	0.480	1.699	0.986	7.106	1.601	6697.07	6198.82	499.06	2.048	7.791
	0.15916	0.936	0.459	0.302	0.477	0.327	3.364	0.710	786.07	785.10	222.47	0.644	0.681
W	0.37937	2.635	0.464	1.272	0.805	1.305	0.914	2.288	5998.10	5797.76	200.00	1.736	7.484
	0.10203	0.593	0.193	0.324	0.204	0.362	0.780	1.442	595.18	614.78	128.68	0.421	0.594

The units of orbital period and temperature are day and Kelvin, respectively. The orbital angular momentum is in a unit of $\times 10^{51}$ cm$^2 \cdot$ g $\cdot$ s^{-1}. The other parameters are in the solar unit. The values in the third and fifth lines denote the standard derivations of the corresponding parameters.
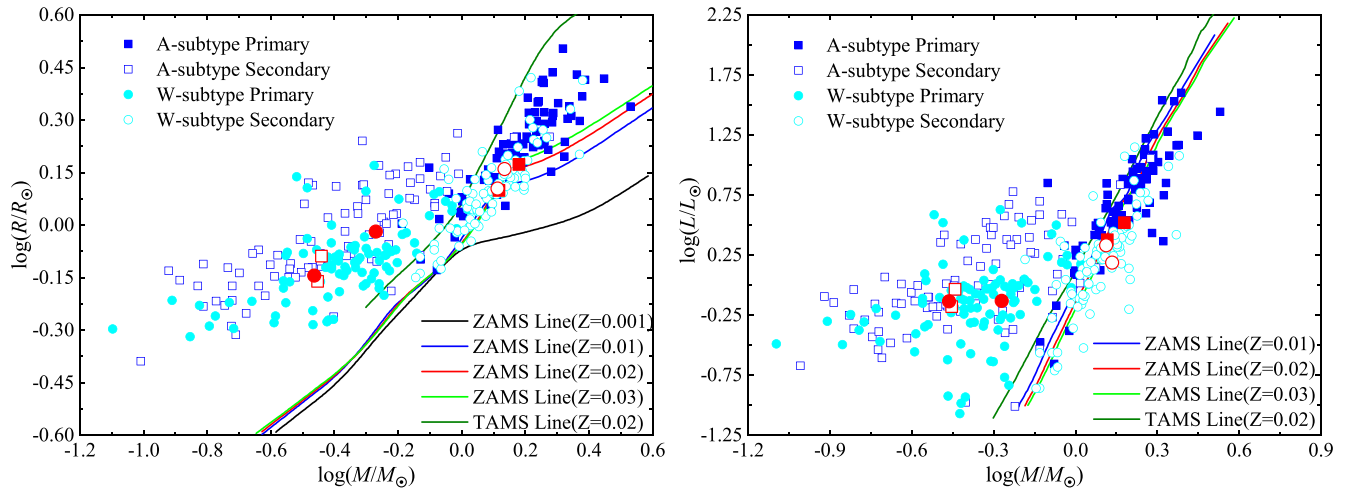
Figure 8. Mass-Radius (left panel), and Mass-Luminosity (right panel) diagrams. The ZAMS lines with different metallicities and TAMS line are calculated for single main-sequence stars using PARSEC models (Bressan et al. 2012). The filled and open squares denote the primary and secondary components of A-subtype samples, respectively. The filled and open circles denote the primary and secondary components of W-subtype samples, respectively. The primary and secondary components for our four targets are depicted as the corresponding red symbols with somewhat larger size.

evolutionary path for the two different subtypes. For instance, the close detached binaries with different initial states may evolve independently into either A- or W-subtype contact binaries (Zhang, Qian, & Liao 2020). Also, the close detached binaries evolve in a similar way but with different mass/energy transfer rate and/or different mass/angular momentum loss rate, leading to different evolutionary outcomes (Gazeas & Stępień 2008). Moreover, we cannot exclude the possibility that some A-subtype systems with small angular momentum have evolved from W-subtype systems, while others (with relatively large angular momentum) have evolved directly from near-contact binaries (Yakut & Eggleton 2005).

6. Conclusion

In this paper, we performed the first photometric and orbital period investigations for four W UMa-type contact binaries: V473 And, V805 And, LQ Com, and EG CVn. Also, we analysed their current states of evolution and made a simple statistical study based on the physical parameters of nearly 200 contact binaries. From these investigations, we could draw out several following conclusions:

(1) V805 And and LQ Com are the total eclipsing binaries, while V473 And and EG CVn is the partial eclipsing one. V473 And and LQ Com belong to the A subtype of W UMa-type contact binaries, while V805 And and EG CVn belong to the W-subtype.

(2) The light curves of V805 And, LQ Com, and EG CVn show a weak O'Connell effect which may be interpreted as a result of the cool spot on their primary components.

(3) With two distinct methods, the absolute parameters for four targets have been well estimated.

(4) All four targets show cyclic period variations which may be caused by either the light-time effect of the third body or the cyclic magnetic activity. In addition, due to mass transfer, three systems: V473 And, V805 And, and EG CVn, are undergoing a secular period decrease and increase, respectively.

(5) A statistical study suggested that the W-subtype contact binaries should be more evolved than the A-subtype ones. Furthermore, it is possible that some W-subtype systems have been evolved from the A-subtype systems, but the opposite direction seems to be physically difficult.

Finally, it should be mentioned that two conclusions: the W subtype of EG CVn and the possible evolution direction of A-subtype contact binaries to W-subtype systems, are rather dubious. Although our photometric solutions for EG CVn derived from both TESS and our ground-based observations, suggested that EG CVn is a W-subtype contact binary, we should note that the difference between two eclipse depths of its light curves is very small, even smaller than the error of photometric data, indicating an almost equal temperatures of the primary and secondary components. Thus, it would be not very reliable that the primary star is somewhat cooler than the secondary star. Moreover,

according to the statistical conclusion of Qian (2001), the W-subtype contact binaries with a high mass ratio[p] ($q' > 0.4$) usually show a secular period increase, while the orbital periods of the low-mass-ratio ($q' < 0.4$) systems are undergoing a secular decrease. Among our two W-subtype systems, V805 And seems follow to the conclusion, while EG CVn breaks this rule because it has a low mass ratio ($q' = 1/q = 0.27$), and shows a secular period increase. However, another statistical analysis for secular variations in the orbital periods of 73 contact binaries suggested that these systems were divided roughly equally between the secular increase and decrease of their orbital periods, regardless of the mass ratio (Dryomova & Svechnikov 2006). This result does not support the conclusion of Qian (2001). Moreover, the equal division plausibly indicated mass might be transferred alternately from one component to the other, just as predicted by the thermal relaxation oscillation theory (Lucy 1976; Flannery 1976). For the latter, the statistical differences of physical parameters between two subtypes, perhaps, are originated from the insufficient samples of two subtypes. In a word, the two conclusions should be open to question and needed to be further studied observationally and theoretically.

References

Akerlof, C., et al. 2000, AJ, 119, 1901

Andronov, N., Pinsonneault, M. H., & Terndrup, D. M. 2006, ApJ, 646, 1160

Applegate, J. H. 1992, ApJ, 385, 621

Banfi, M., et al. 2012, IBVS, 6033, 1

Bellm, E. C., et al. 2019, PASP, 131, 018002

Bilir, S., Karataş, Y., Demircan, O., & Eker, Z. 2005, MNRAS, 357, 497

Binnendijk, L. 1970, Vistas in Astronomy, 12, 217

Blattler, E., & Diethelm, R. 2002, IBVS, 5269, 1

Borkovits, T., Érdi, B., Forgács-Dajka, E., & Kovács, T. 2003, A&A, 398, 1091

Borkovits, T., Csizmadia, S., Forgács-Dajka, E., & Hegedüs, T. 2011, A&A, 528, A53

Borkovits, T., Rappaport, S., Hajdu, T., & Sztakovics, J. 2015, MNRAS, 448, 946

Borkovits, T., Hajdu, T., Sztakovics, J., Rappaport, S., Levine, A., Bró, I. B., & Klagyivik, P. 2016, MNRAS, 455, 4136

Brat, L., et al. 2011, OEJV, 137, 1

Bressan, A., Marigo, P., Girardi, L., Salasnich, B., Dal Cero, C., Rubele, S., & Nanni, A. 2012, MNRAS, 427, 127

Brinkworth, C. S., Marsh, T. R., Dhillon, V. S., & Knigge, C. 2006, MNRAS, 365, 287

Butters, O. W., et al. 2010, A&A, 520, L10

Carter, J. A., et al. 2011, Science, 331, 562

Claret, A. 2017, A&A, 600, A30

Claret, A., & Bloemen, S. 2011, A&A, 529, A75

Corfini, G., et al. 2014, IBVS, 6094, 1

Counselman Charles, C. I. 1973, ApJ, 180, 307

Darwin, G. H. 1908, PRSLSA, 80, 166

Diaz-Cordoves, J., & Gimenez, A. 1992, A&A, 259, 227

Diethelm, R. 2001, IBVS, 5060, 1

Diethelm, R. 2003, IBVS, 5438, 1

Diethelm, R. 2004, IBVS, 5543, 1

Diethelm, R. 2005, IBVS, 5653, 1

Diethelm, R. 2006, IBVS, 5713, 1

Diethelm, R. 2007, IBVS, 5781, 1

Diethelm, R. 2009, IBVS, 5894, 1

Diethelm, R. 2011, IBVS, 5960, 1

Diethelm, R. 2013, IBVS, 6042, 1

Drake, A. J., et al. 2009, ApJ, 696, 870

Dryomova, G. N., & Svechnikov, M. A. 2006, Ap, 49, 358

Eggleton, P. P. 2012, JASS, 29, 145

Eggleton, P. P., & Tokovinin, A. A. 2008, MNRAS, 389, 869

Fabrycky, D., & Tremaine, S. 2007, ApJ, 669, 1298

Flannery, B. P. 1975, MNRAS, 170, 325

Flannery, B. P. 1976, ApJ, 205, 217

Gaia Collaboration, et al. 2016, A&A, 595, A1

Gaia Collaboration, et al. 2018, A&A, 616, A1

Gazeas, K. D. 2009, CoAst, 159, 129

Gazeas, K. D., & Niarchos, P. G. 2006, MNRAS, 370, L29

Gazeas, K., & Stępień, K. 2008, MNRAS, 390, 1577

Guinan, E. F., & Bradstreet, D. H. 1988, in NATO Advanced Study Institute (ASI) Series C, Vol. 241, Formation and Evolution of Low Mass Stars, ed. A. K. Dupree, & M. T. V. T. Lago, 345

Hajek, P. 2006, JAVSO, 35, 222

Han, Z., Podsiadlowski, P., Maxted, P. F. L., Marsh, T. R., & Ivanova, N. 2002, MNRAS, 336, 449

Henden, A. A., Levine, S., Terrell, D., & Welch, D. L. 2015, in American Astronomical Society Meeting Abstracts #225, 336.16

Hilditch, R. W. 1989, Space Sci. Rev., 50, 289

Hilditch, R. W., King, D. J., & McFarlane, T. M. 1988, MNRAS, 231, 341

Honková, K., et al. 2014, OEJV, 165, 1

Honkova, K., et al. 2015, OEJV, 168, 1

Hoňková, K., et al. 2013, OEJV, 160, 1

Hu, K., Chen, K., Xiang, F.-Y., Yu, Y.-X., & Zhao, E.-G. 2019, AJ, 158, 104

Hu, K., Jiang, Z.-H., Yu, Y.-X., & Xiang, F.-Y. 2018, New A, 62, 20

Hu, K., Yu, Y.-X., Zhang, J.-F., & Xiang, F.-Y. 2020, AJ, 160, 62

Hubscher, J. 2014, IBVS, 6118, 1

Hubscher, J. 2016, IBVS, 6157, 1

Hubscher, J. 2017, IBVS, 6196, 1

Hubscher, J., Braune, W., & Lehmann, P. B. 2013, IBVS, 6048, 1

Hubscher, J., Lehmann, P. B., Monninger, G., Steinbach, H.-M., & Walter, F. 2010, IBVS, 5918, 1

Hubscher, J., Lehmann, P. B., & Walter, F. 2012, IBVS, 6010, 1

Hubscher, J., & Monninger, G. 2011, IBVS, 5959, 1

Hut, P. 1980, A&A, 92, 167

Irwin, J. B. 1952, ApJ, 116, 211

Jayasinghe, T., et al. 2018, MNRAS, 477, 3145

Jayasinghe, T., et al. 2019, MNRAS, 486, 1907

Juryšek, J., et al. 2017, OEJV, 179, 1

Kähler, H. 2002, A&A, 395, 899

Kähler, H. 2004, A&A, 414, 317

Kim, C.-H., Jeong, J. H., Demircan, O., Muyesseroglu, Z., & Budding, E. 1997, AJ, 114, 2753

Kiseleva, L. G., Eggleton, P. P., & Mikkola, S. 1998, MNRAS, 300, 292

Kjurkchieva, D., & Vasileva, D. 2015, PASA, 32, e023

Kjurkchieva, D. P., Popov, V. A., Eneva, Y., & Petrov, N. I. 2019, RAA, 19, 014

Kozai, Y. 1962, AJ, 67, 591

Kuzmin, M. L. 2008, PZP, 8, 15

Kwee, K. K., & van Woerden, H. 1956, Bull. Astron. Inst. Netherlands, 12, 327

Lanza, A. F., & Rodonò, M. 2002, AN, 323, 424

Lanza, A. F., Rodono, M., & Rosner, R. 1998, MNRAS, 296, 893

Li, L., Han, Z., & Zhang, F. 2004, MNRAS, 351, 137

Li, L., Zhang, F., Han, Z., Jiang, D., & Jiang, T. 2008, MNRAS, 387, 97

Li, K., et al. 2021, AJ, 162, 13

Lim, J., & White, S. M. 1996, ApJ, 462, L91

Liu, L., Qian, S., Li, K., He, J., Li, L., Zhao, E., & Li, X. 2020, Ap&SS, 365, 71

Lucy, L. B. 1967, ZAp, 65, 89

Lucy, L. B. 1968, ApJ, 151, 1123

Lucy, L. B. 1973, Ap&SS, 22, 381

Lucy, L. B. 1976, ApJ, 205, 208

Maceroni, C., & van't Veer, F. 1996, A&A, 311, 523

Masci, F. J., et al. 2019, PASP, 131, 018003

McCartney, S. 1997, in Astronomical Society of the Pacific Conference Series, Vol. 130, The Third Pacific Rim Conference on Recent Development on Binary Star Research, ed. K.-C. Leung, 129

Mochnacki, S. W. 1981, ApJ, 245, 650

Moses, A. P. 1976, MNRAS, 176, 161

Mullan, D. J., Doyle, J. G., Redman, R. O., & Mathioudakis M. 1992, ApJ, 397, 225

Nelson, R. H. 2002, IBVS, 5224, 1

Nelson, R. H. 2008, IBVS, 5820, 1

Nelson, R. H. 2009, IBVS, 5875, 1

Nelson, R. H. 2019, IBVS, 6262, 1

O'Connell, D. J. K. 1951, Publications of the Riverview College Observatory, 2, 85

Paczyński, B. 1971, ARA&A, 9, 183

Paczyński, B., Szczygieł, D. M., Pilecki, B., & Pojmański, G. 2006, MNRAS, 368, 1311

Pagel, L. 2018, IBVS, 6244, 1

Pagel, L. 2020, BAVJ, 033, 1

Paschke, A. 2019, BAVJ, 031, 1

Pecaut, M. J., & Mamajek, E. E. 2013, ApJS, 208, 9

Pribulla, T., Kreiner, J. M., & Tremko, J. 2003, Contributions of the Astronomical Observatory Skalnate Pleso, 33, 38

Qian, S. 2001, MNRAS, 328, 635

Qian, S. 2003, MNRAS, 342, 1260

Qian, S., Yang, Y., Zhu, L., He, J., & Yuan, J. 2006, Ap&SS, 304, 25

Rappaport, S., Deck, K., Levine, A., Borkovits, T., Carter, J., El Mellah, I., Sanchis-Ojeda, R., & Kalomeni B. 2013, ApJ, 768, 33

Ricker, G. R., et al. 2015, JATIS, 1, 014003

Ruciński, S. M. 1969, AcA, 19, 245

Rucinski, S. M. 1974, AcA, 24, 119

Rucinski, S. M. 1985, in Interacting Binary Stars, ed. J. E. Pringle, & R. A. Wade (Cambridge University Press), 85

Rucinski, S. M. 1993, in Astrophysics and Space Science Library, Vol. 177, Astrophysics and Space Science Library, ed. J. Sahade, G. E. McCluskey, & Y. Kondo, 111, doi: 10.1007/978-94-011-2416-4_8

Rucinski, S. M. 1998, AJ, 116, 2998

Rucinski, S. M. 2000, AJ, 120, 319

Schlafly, E. F., & Finkbeiner, D. P. 2011, ApJ, 737, 103

Shappee, B. J., et al. 2014, ApJ, 788, 48

Skrutskie, M. F., et al. 2006, AJ, 131, 1163

Smith, R. C. 1984, QJRAS, 25, 405

Socia, Q. J., et al. 2020, AJ, 159, 94

Soderhjelm, S. 1975, A&A, 42, 229

Stępień, K. 2004, in Vol. 219, Stars as Suns: Activity, Evolution and Planets, ed. A. K. Dupree, & A. O. Benz, 967

Terrell, D., & Wilson, R. E. 2005, Ap&SS, 296, 221

Tokovinin, A., Thomas, S., Sterzik, M., & Udry, S. 2006, A&A, 450, 681

Tylenda, R., et al. 2011, A&A, 528, A114

Van Hamme, W., & Wilson, R. E. 2007, ApJ, 661, 1129

Vrastak, M. 2015, OEJV, 169, 23

Webbink, R. F. 1976, ApJ, 209, 829

Webbink, R. F. 2003, in Astronomical Society of the Pacific Conference Series, Vol. 293, 3D Stellar Evolution, ed. S. Turcotte, S. C. Keller, & R. M. Cavallo, 76 (arXiv:astro-ph/0304420)

Weber, E. J., & Davis, L. J. 1967, ApJ, 148, 217

Wilson, R. E. 1979, ApJ, 234, 1054

Wilson, R. E. 1990, ApJ, 356, 613

Wilson, R. E., & Devinney, E. J. 1971, ApJ, 166, 605

Wilson, R. E., & Van Hamme, W. 2014, ApJ, 780, 151

Woźniak, P. R., et al. 2004, AJ, 127, 2436

Yakut, K., & Eggleton, P. P. 2005, ApJ, 629, 1055

Yang, Y.-G., & Qian S.-B. 2015, AJ, 150, 69

Yao, X., et al. 2015, AJ, 150, 107

Yıldız, M. 2014, MNRAS, 437, 185

Yu, Y.-X., Li, Q., Huang, H.-P., Hu, K., & Xiang, F.-Y. 2022, New A, 91, 101695

Zejda, M. 2006, JAVSO, 35, 211

Zhai, D. S., & Fang, M. J. 1995, AcASn, 36, 46

Zhang, J., Qian, S.-B., & He, J.-D. 2017a, RAA, 17, 22

Zhang, J., Qian, S.-B., Han, Z.-T., & Wu, Y. 2017b, MNRAS, 466, 1118

Zhang, X.-D., Qian, S.-B., & Liao, W.-P. 2020, MNRAS, 492, 4112

Zhou, D.-Q., & Leung, K.-C. 1990, ApJ, 355, 271

Zhu, L. Y., Qian, S. B., Zola, S., & Kreiner, J. M. 2009, AJ, 137, 3574

Zhu, L.-Y., Zhao, E.-G., & Zhou, X. 2016, RAA, 16, 68